

DRI File Copy

ESD ACCESSION LIST

DRI Call No. 77798

Copy No. 1 of 1 cys.

Technical Note

1972-25

**Radar Cross Section
of a Pyramid with Nodes**

W. H. Schoendorf

16 November 1972

Prepared for the Department of the Air Force
under Electronic Systems Division Contract F19628-73-C-0002 by

Lincoln Laboratory

MASSACHUSETTS INSTITUTE OF TECHNOLOGY

LEXINGTON, MASSACHUSETTS



AD753684

ESD RECORD COPY

RETURN TO
SCIENTIFIC & TECHNICAL INFORMATION DIVISION
(DRI), Building 1435

Approved for public release; distribution unlimited.

MASSACHUSETTS INSTITUTE OF TECHNOLOGY
LINCOLN LABORATORY

RADAR CROSS SECTION OF A PYRAMID WITH NODES

W. H. SCHOENDORF

Group 92

TECHNICAL NOTE 1972-25

16 NOVEMBER 1972

Approved for public release; distribution unlimited.

LEXINGTON

MASSACHUSETTS

The work reported in this document was performed at Lincoln Laboratory, a center for research operated by Massachusetts Institute of Technology, with the support of the Department of the Air Force under Contract F19628-73-C-0002.

This report may be reproduced to satisfy needs of U.S. Government agencies.

ABSTRACT

High-frequency scattering by a perfectly conducting N-noded pyramid is investigated. The principally polarized radar cross section is derived by integrating the fields scattered from a wedge around the base termination and, also, the longitudinal edges. The theoretical results are compared with measurements and shown to be in reasonable agreement.

Accepted for the Air Force
Joseph J. Whelan, USAF
Acting Chief, Lincoln Laboratory Liaison Office

1. INTRODUCTION

The radar cross section (RCS) of a perfectly conducting, noded, conically shaped body in the high frequency limit is treated in this report. The cross section of this body in the plane normal to its longitudinal axis is "star shaped", as shown in Fig. 1. A photograph of a three- and four-noded body is shown in Fig. 2. This generic shape will henceforth be referred to as an N-noded pyramid with N denoting the number of convex nodes.

The scattered fields will be determined by extending Ross's¹ modification of Keller's² geometrical theory of diffraction (GTD) to aspect angles beyond the pyramid half-angle. GTD is an asymptotic theory, valid at small wavelengths, which allows for the description of diffracted rays produced at an edge or a tip. Since the wavelengths are small, the diffraction phenomenon is local in nature, which suggests that the structure of the diffracted fields can be determined from simpler problems in which only the local geometrical and physical properties enter. These "canonical" problems are solved in order to determine the diffraction coefficients which are the ratio of the diffracted and incident fields.

Keller³ has employed GTD to obtain the RCS of a finite circular cone. Specular reflection from this object occurs when the aspect angle is equal to π or $\frac{\pi}{2} - \gamma$, where γ is the cone half angle. The backscattered rays for other aspect angles are produced by tip-, rear edge-, and surface-diffracted rays. The field on a ray diffracted by the tip is proportional to λ , that on a ray diffracted from the rear edge is proportional to $\lambda^{\frac{1}{2}}$, and that on a surface diffracted ray decreases exponentially with λ^{-1} . Thus, for small wavelengths the edge-diffracted rays provide the dominant return. A modification of Fermat's principle indicates that rays diffracted by an edge lie on a cone with half-angle equal to the angle between the incident ray and the edge, when both rays lie in the same medium. The diffracted and incident rays lie

on opposite sides of the plane normal to the edge at the point of diffraction. It is apparent, therefore, that the points on the rear edge of the cone at which the positive tangent is perpendicular to the direction of propagation are the only contributors to the backscattered field. At nose-on incidence (zero aspect angle), each point on the ring discontinuity at the base of the cone contributes to the backscattered return, and the GTD results must be modified by a caustic correction. An incremental increase in the aspect angle results in two localized edge scattering centers on the base and, therefore, a discontinuity in the diffraction formulation.

This situation may be remedied by integrating the edge diffracted fields around the rim of the cone. This concept was used by Raybin⁴ to obtain the RCS of spherical shell segments and by Ross¹ to obtain the RCS of a finite cone for aspect angles smaller than the cone half-angle. A similar technique is employed in the present work to obtain the RCS of the noded pyramid.

The RCS of the pyramid, assuming contributions from the rear edges alone, is derived in Section II. A comparison of the predictions of this section with static measurements is presented in Section III. The contributions of the longitudinal edges are investigated in Section IV, and the last section is devoted to conclusions.

II. THEORETICAL PREDICTIONS

The RCS of the pyramid will first be approximated by considering simply the return from the rim discontinuity at the rear of the target. This technique was employed previously on a similar target with rounded sides, and it provided adequate results for small aspect angles.⁵

Consider a noded pyramid of outer base radius a , inner base radius b , and length L measured along an axis normal to its base and passing through the vertex. The base outline shown in Fig. 1 indicates that the edges and angles of

interest are ordered sequentially from 0 to $2N-1$ in a counter-clockwise direction in the x - y plane. The scattering geometry employed in these calculations is depicted in Fig. 3, where the aspect angle Ψ is the angle between the incident wave vector, \hat{k} , and the longitudinal body axis, which is oriented along the z axis. The angle β is the angle between the projection of \hat{k} in the x - y plane and the positive x axis, and is used to indicate the roll orientation of the target.

The major assumption at this point is that the base of the target provides the dominant return at high frequencies. The backscattered field is obtained by approximating this rim discontinuity by a series of flat convex wedges and then adding the backscattered field from each wedge, accounting for the wedge orientation. The appropriate expression for the total backscattered field is⁴

$$U^S = \frac{1}{\lambda R} \int_{\text{ill.}} U^i e^{ik\rho} f(\Psi, \beta, x) d\ell \quad (1)$$

where U^S is the scattered field, U^i is the incident field at the integration point, k is the wavenumber ($\frac{2\pi}{\lambda}$), ρ is the distance between the observer and the integration point, R the distance from the origin to the observer. The position of the diffraction point, P , on the base of the target is described in terms of the variable x . The function $f(\Psi, \beta, x)$ characterizes the scattering properties of the base discontinuity and can be defined within the framework of GTD as¹

$$f(\Psi, \beta, x) = e^{-i\pi/4} \sqrt{\lambda} D(\Psi, \beta, x) \quad (2)$$

where the diffraction coefficient $D(\Psi, \beta, x)$ is obtained from the solution of the appropriate canonical scattering problem, which is the two-dimensional wedge for the case of interest. The integration is carried out over the illuminated portion of the rim discontinuity with $d\ell$ being an incremental length along this path.

The wedge used for the calculation of the diffraction coefficient is defined by passing a plane through the diffraction point P, on the base of the pyramid, that is normal to the tangent to the rim of the pyramid in the x-y plane. The intersection of this normal plane with the back of the pyramid is a straight line denoted by PL, while its intersection with the slant surface of the pyramid is another line denoted by PM. The diffraction effects at the point P are described as if there were an infinite wedge bounded by the lines PL and PM.

The expression for the diffraction coefficient for this wedge is given by³

$$D_{\perp \parallel} = \frac{e^{i\pi/4} \sin(\frac{\pi}{\nu})}{\nu \sqrt{2\pi k} \sin \delta} \left\{ \left[\cos \frac{\pi}{\nu} - \cos \frac{2\varphi}{\nu} \right]^{-1} \pm \left[\cos \frac{\pi}{\nu} - 1 \right]^{-1} \right\} . \quad (3)$$

The angle between the projection of the incident ray in the normal plane and the edge PM is denoted by φ , while δ is the angle between the direction of propagation and the positive tangent to the edge. The upper and lower signs refer to the cases when the incident polarization is perpendicular and parallel to the edge of the wedge, respectively. The quantity ν is given by

$$\nu = \frac{2\pi - \Omega}{\pi} \quad (4)$$

where Ω is the angle between PL and PM (i.e., the interior wedge angle). This quantity is given by

$$\cos \Omega = ab \sin \frac{\pi}{N} \left[a^2 b^2 \sin^2 \frac{\pi}{N} + L^2 (a^2 + b^2 - 2ab \cos \frac{\pi}{N}) \right]^{-1/2} \quad (5)$$

The diffraction coefficient must be evaluated at each point of the rim so that the angles φ and δ must be expressed as functions of Ψ , β , and x . Since the

polarization conventions of equation (3) apply to the local conditions at each integration point on the ring it is necessary to transfer this convention to the reference frame of the radar. Vertical polarization is defined as the case when the incident and scattered fields lie in the x-y plane and the vertically polarized incident field is given by

$$\hat{e}_v = \hat{x} \sin \beta - \hat{y} \cos \beta \quad (6)$$

The horizontally polarized incident field is then directed normal to the propagation vector \hat{k} and \hat{e}_v and is given by

$$\hat{e}_h = \hat{x} \cos \Psi \cos \beta + \hat{y} \cos \Psi \sin \beta - \hat{z} \sin \Psi \quad (7)$$

The circularly polarized incident field is formed by the addition of \hat{e}_h and \hat{e}_v with the latter shifted in phase by 90 degrees.

The appropriate expressions for the principally polarized backscattered returns for each polarization may be written as

$$\vec{E}_{v,h,c}(s) = \hat{e}_{v,h,c} \frac{e^{-1\pi/4} e^{ikR}}{R \sqrt{\lambda}} \int_{\text{ill.}} D_{v,h,c} e^{2ikg} d\ell \quad (8)$$

where

$$\begin{aligned} D_v &= (D_{||} - D_{\perp}) P^2 + D_{\perp} \\ D_h &= (D_{||} - D_{\perp}) Q^2 \cos^2 \Psi + D_{\perp} \\ D_c &= \frac{1}{2}(D_{||} - D_{\perp}) (1 - Q^2 \sin^2 \Psi) + D_{\perp} \end{aligned} \quad (9)$$

and

$$g = L \cos \Psi - c_j \sin \Psi \sin \beta - \sin \Psi (\cos \beta + m_j \sin \beta) x. \quad (10)$$

The functions P and Q are given by

$$P = t_x \sin \beta - t_y \cos \beta \quad (11a)$$

$$Q = t_x \cos \beta + t_y \sin \beta \quad (11b)$$

where t_x and t_y are the x and y components of the vector tangent to the rim of the pyramid. The parameters c_j and m_j in Eq. (10) are the y intercept and slope of the j^{th} edge, respectively, while x , the integration variable, refers to the x coordinate of the diffraction point P.

Evaluation of Eq. (8) over the illuminated portion of the base of the pyramid leads to the following expressions for the RCS of the body

$$\sigma = \frac{\lambda^2}{16\pi^3} \left| \sum_{j=0}^{2N-1'} \text{sgn } \phi_j (1 + m_j^2)^{1/2} e^{2ik\xi_j \Delta_j} \left(e^{-2ik\xi_j x_1(j)} - e^{-2ik\xi_j x_2(j)} \right) \xi_j^{-1} \right|^2 ; \Psi \neq 0 \quad (12a)$$

$$\sigma = \frac{1}{\pi} \left| \sum_{j=0}^{2N-1} \text{sgn } \phi_j (1 + m_j^2)^{1/2} \Delta_j (x_1(j) - x_2(j)) \right|^2 ; \Psi = 0 \quad (12b)$$

The prime on the sum indicates that the sum is carried out over the edges that are partially or completely illuminated. The function $\text{sgn } \phi_j$ is given by

$$\text{sgn } \phi_j = \begin{cases} +1, & \phi_j > 0 \\ -1, & \phi_j < 0 \end{cases} \quad (13)$$

where

$$\phi_j = \begin{cases} b \cos \theta_{j+1} - a \cos \theta_j, & j \text{ even}, \\ a \cos \theta_{j+1} - b \cos \theta_j, & j \text{ odd}, \end{cases} \quad (14)$$

and $\theta_j = \frac{\pi j}{N}$.

The functions ξ_j and ζ_j are given by

$$\xi_j = L \cos \Psi - c_j \sin \Psi \sin \beta \quad (15)$$

$$\zeta_j = \sin \Psi [\cos \beta + m_j \sin \beta]. \quad (16)$$

The Δ_j are the polarization dependent parameters in the solution and are given by

$$\Delta_j = \alpha_j [\gamma_j (1 - 2Q_j^2 \cos^2 \Psi) + \epsilon_j] \quad \text{Horizontal Polarization} \quad (17a)$$

$$\Delta_j = \alpha_j [\gamma_j (1 - 2P_j^2) + \epsilon_j] \quad \text{Vertical Polarization} \quad (17b)$$

$$\Delta_j = \alpha_j [\gamma_j Q_j^2 \sin^2 \Psi + \epsilon_j] \quad \text{Circular Polarization} \quad (17c)$$

where

$$\alpha_j = v^{-1} (1 - Q_j^2 \sin^2 \Psi)^{-1/2} \sin \frac{\pi}{v}, \quad (18a)$$

$$\gamma_j = \left[\cos \frac{\pi}{v} - 1 \right]^{-1} \quad (18b)$$

and

$$\epsilon_j = \left[\cos \frac{\pi}{v} - \cos \frac{2\varphi_j}{v} \right]^{-1} . \quad (18c)$$

The P_j and Q_j are the values of P and Q in Eq. (11) evaluated on the j^{th} edge and

$$\varphi_j = \cos^{-1} \left\{ \left[1 + \frac{L^2 K_1^2}{K_2^2} \right]^{-1/2} \left[1 - Q_j^2 \sin^2 \Psi \right]^{-1/2} \left[P_j \sin \Psi + \frac{LK_1}{K_2} \cos \Psi \right] \right\} \quad (19)$$

where

$$K_1 = (a^2 + b^2 - 2ab \cos \frac{\pi}{N})^{1/2} \quad (20)$$

and

$$K_2 = ab \sin \frac{\pi}{N} . \quad (21)$$

The illuminated portion of the j^{th} edge is bounded by the x coordinates $x_1(j)$ and $x_2(j)$. The results of reference (5) indicate that a good correlation between theoretical and experimental results is obtained by assuming that the rim of the pyramid is completely illuminated for aspect angles extending to the pyramid half-angle. This assumption is not strictly correct in the geometrical optics limit, as the longitudinal and rear edges of the pyramid create a shadow boundary for smaller values of Ψ . (A description of this shadowing effect is given in Appendix I.)

Since the wavelength of the incident radiation is not infinitesimally small, however, the shadow boundary is not a sharp discontinuity and the base of the pyramid may be considered to be fully illuminated for values of ψ extending beyond the pyramid half-angle. The parameters $x_1(j)$ and $x_2(j)$ may be written as

$$\left. \begin{aligned} x_1(j) &= a \cos \theta_{j+1} \\ x_2(j) &= b \cos \theta_j \end{aligned} \right\} \quad j \text{ odd}, \quad (22a)$$

and

$$\left. \begin{aligned} x_1(j) &= b \cos \theta_{j+1} \\ x_2(j) &= a \cos \theta_j \end{aligned} \right\} \quad j \text{ even}. \quad (22b)$$

III. EXPERIMENTAL RESULTS

A three- and a four-noded pyramid were fabricated and measured on the Lincoln Laboratory indoor antenna range. The dimensions of the targets are shown in Table 1. The measurements are accurate to within 2 dB.

TABLE 1
TARGET DIMENSIONS

<u>N</u>	<u>L (in.)</u>	<u>a (in.)</u>	<u>b (in.)</u>	<u>Half Angle (degrees)</u>
3	24.000	3.550	0.935	8
4	24.000	3.550	1.460	8

Vertical and horizontal principally polarized measurements were performed at 1.00, 3.00, and 4.03 GHz, while principally polarized circular measurements were obtained at 4.03 GHz. These measurements were conducted over a variety of body roll orientations, with zero degree roll orientation corresponding to one of the nodes directed upwards. The target roll is accomplished by a rotation of the pyramid about the z axis in a positive right handed sense.

Since the geometry shown in Fig. 3 corresponds to a stationary target and movable radar, and the measurements were performed by rotating the target in a horizontal plane in front of a stationary antenna, it is necessary to transform the coordinate system of Fig. 3 to the actual range geometry. This is easily accomplished by defining β in the following manner:

$$\beta = \begin{cases} \frac{\pi}{2} - \theta_R, & \Psi > 0 \\ -\frac{\pi}{2} - \theta_R, & \Psi < 0 \end{cases} \quad (23a)$$

$$(23b)$$

where θ_R is the roll orientation, and Ψ the aspect angle retains its previous definition. Positive values of Ψ correspond to the target pointing to the left of the radar as seen from behind the antenna.

The data on the three-noded pyramid will be presented at 0° , 30° , and 60° roll angle while that of the four-noded pyramid is shown at 0° and 45° roll orientations. The theoretical predictions are obtained by using Eqs. 12a and 12b and assuming that the rear edges remain completely illuminated throughout the entire aspect angle range shown.

The results for the three-noded target will be considered first. The return from this target will be symmetrical in Ψ about $\Psi=0^\circ$ for the 0° and 60° roll orientations. The 4.03 GHz measured and predicted returns are shown in Figs. 4, 5, and 6 for circular, horizontal, and vertical polarizations, respectively.

Figure 4 indicates that the circularly polarized predictions are within 2 dB of the measured values out to an aspect angle of 12° for the 0° and 60° roll orientations. The error increases slightly for negative values of Ψ for the unsymmetrical 30° orientation, while the results are quite reasonable out to 24° for positive values of Ψ .

The horizontal polarization predictions shown in Fig. 5 provide a very good estimate of the measured RCS out to an aspect angle of 18° for the symmetrical 0° and 60° roll orientations. It is seen that, at the 30° roll orientation, the predictions remain within 2 dB of the data for an aspect angle range of $\pm 12^\circ$.

The vertical polarization predictions shown in Fig. 6 do not provide a reasonable estimate of the measured RCS for as large an aspect angle range as those of the previously described polarizations. At all roll orientations there is approximately a 4 dB difference between the predictions and measurements at the endpoint of an 8° aspect angle variation. It should be recalled that the pyramid half angle is approximately 8° . The discrepancy between theory and experiment does not exceed 4 dB within this interval.

The 3.0 GHz horizontally and vertically polarized results are shown in Figs. 7 and 8, respectively. The predictions for horizontally polarized illumination are quite good at the roll angles shown for an aspect angle variation of 20° . The theoretical results fail at the point where the measurements indicate a sharp null. The predictions at the 0° and 60° roll orientations indicate a decrease in RCS at this point, but they do not depict the proper rate of reduction of the RCS.

The vertically polarized predictions displayed in Fig. 8 are within a few dB of the measured results for an aspect angle extent of 12° . However, as in the case of the 4.03 MHz results, the rate of decay of the theoretical RCS is much greater than that of the measurements as the aspect angle increases.

The 1.0 GHz results are shown in Figs. 9 and 10. These results show very little dependence on roll angle. The measured and predicted returns display very little aspect angle variation for an aspect angle interval of 30° . The theoretical results fall a few dB below the measured RCS, but this discrepancy can be partially accounted for by the measurement error. This agreement of the high frequency predictions with the measurements at 1 GHz is not completely unexpected and was noted previously.⁵

The measurements and theoretical predictions for the four-noded pyramid are presented at roll orientations of 0° and 45° . The return from this target at these orientations is symmetrical in Ψ about $\Psi = 0^{\circ}$ for both roll orientations. The theoretical RCS is obtained from Eqs. 12a and 12b assuming, as in the case of the three-noded pyramid, that the rear edges remain completely illuminated throughout the entire aspect angle interval shown.

The principally polarized measurements and predictions at 4.03 GHz for incident circular, horizontal, and vertical illumination are shown in Figs. 11, 12, and 13, respectively.

Figure 11 indicates that the circularly polarized predictions are within 2 dB of the measured returns out to an aspect angle of 12° . As in the case of the three-noded target, the discrepancy between the measured and theoretical values at circular polarization becomes large when the measured RCS displays a null or a local minimum. It is seen in Fig. 11b that the calculations display an increase in the return, which initiates at 13° and is also observed in the measured values. The predicted and measured results then tend to diverge from each other again at about 18° .

The horizontally polarized results are shown in Fig. 12. The measurements and predictions stay within a few dB of each other out to about 18° for the 0° roll orientation. When the target is rolled 45° , the predictions diverge from the

measured results at a smaller aspect angle. The predictions indicate a null at 11° , while the measurements show a local minimum occurring at 19° . The predicted null is followed by an increase in RCS value, which approaches the measurements again at 24° .

The quality of the vertically polarized predictions shown along with the measurements in Fig. 13 is very dependent on the roll angle orientation. At the 0° roll orientation the predictions indicate a large divergence from the measured results when the aspect angle has reached 8° . When the target is rolled 45° , the predictions remain very close to the measurements out to an aspect angle of 12° , where the measurements display a local minimum and the predictions fall well below the measured values. However, the calculations show an increase initiating at 16° , which is similar to the rise shown by the measurements; and the ensuing lobe, which extends from 16° to 30° , is similar in position to that observed in the measurements.

The 3.0 GHz results are shown in Figs. 14 and 15 for the horizontal and vertical polarizations, respectively. In the case of the 0° roll orientation, the horizontal predictions are quite good out to an aspect angle of 19° . At this point, the rate of decrease of the measured pattern is much greater than that of the calculations. When the target is rolled 45° , the horizontally polarized calculations diverge from the measurements at a smaller aspect angle because of a sharp null predicted at an aspect angle of 15° . The null occurs in the measurements at 23° and is not as deep as the theoretical results indicate. The lobe in the RCS pattern which follows the null is seen in the calculations although its position is shifted by 8° .

The vertically polarized results at 3.0 GHz and 0° and 45° roll orientations are displayed in Fig. 15. At 0° roll, the predictions fall off too rapidly beyond an aspect angle of 8° , which is similar to the results at 4.03 GHz. The predictions at the 45° roll orientation are within a few dB of the measured results through an aspect variation of 14° .

The 1.0 GHz measurements and predictions displayed in Fig. 16 and 17 are similar to those shown for the three-node case. The measured and theoretical RCS's are both insensitive to roll and aspect angle variations, and the theoretical values fall a few dB below the measured results. In the case of the four-noded target, this discrepancy is within the experimental accuracy.

It is seen from the results of this section that a theoretical calculation based on a modification of GTD applied to the rear edges of a noded pyramid, assuming these edges remain completely illuminated, leads, with few exceptions, to good correlation with measurements for values of ka ranging from 7.6 to 1.9. In all cases except the five listed in Table 2, the theoretical return stayed within a few dB of the measured returns for a minimum aspect angle variation of 12° , which is approximately 1.5 times the pyramid half-angle. In many cases, the predicted results were a reasonable approximation of the measured returns for aspect angle intervals extending to 20° . For the five cases listed in Table 2, the calculations were within a few dB of the measured results for a range of 8° , which is the half-angle of the target. These results indicate that the approximations used in reference (5) can be applied to a wider class of targets than first anticipated and can be extended to larger aspect angle intervals.

In order to improve the results discussed above for large aspect angles, an attempt was made to account for the contribution of the slant edges of the pyramid to the total return from the target. This effort is discussed in the following section.

TABLE 2

Cases in which Approximation is good for Aspect Angle Interval Extending to Pyramid Half-Angle

<u>Number of Nodes</u>	<u>Freq. (GHz)</u>	<u>Polarization</u>	<u>Roll Angle</u>
3	4.03	V	$0^{\circ}, 30^{\circ}, 60^{\circ}$
4	4.03	H	45°
4	4.03	V	0°
4	3.00	H	45°
4	3.00	V	0°

IV. CONTRIBUTION OF THE LONGITUDINAL EDGES

In order to improve the theoretical predictions presented in the previous section, the contributions of both the concave and convex longitudinal edges of the pyramid were calculated and included in the RCS formulation. These edges are approximated by N concave and N convex wedges and then treated in a manner similar to that shown in Section II.

The diffraction coefficient for the concave wedge can be obtained from Eq. (3) and may be written as

$$D_{\frac{1}{H}} = \frac{e^{i\pi/4} \sin\left(\frac{\pi - \overline{\Omega}}{\overline{V}}\right)}{\sqrt{2\pi k} \overline{V} \sin \overline{\delta}} \left\{ \left[\cos\left(\frac{\pi - \overline{\Omega}}{\overline{V}}\right) + \cos \frac{2\overline{\varphi}}{\overline{V}} \right]^{-1} \pm \left[1 + \cos\left(\frac{\pi - \overline{\Omega}}{\overline{V}}\right) \right]^{-1} \right\}. \quad (24)$$

The angle between the projection of the incident ray in the normal plane and the nearest wedge face is $\overline{\varphi}$, $\overline{\delta}$ is the angle between the direction of propagation and the positive tangent to the edge; $\overline{\Omega}$ is the interior wedge angle and \overline{V} is given by

$$\overline{V} = \frac{\overline{\Omega}}{\pi} \quad (25)$$

The result of including these longitudinal edges in the total RCS calculation of the pyramid is the addition of two terms to the previous formulation. The RCS may now be written as

$$\sigma = \frac{\lambda^2}{16\pi} 3 \left| H_1 + H_2 + H_3 \right|^2 \quad (26)$$

where H_1 , H_2 , and H_3 are the contributions from the rear, convex, and concave edges, respectively. The quantity H_1 may be obtained from Eq. 12 and is given by

$$H_1 = \frac{4\pi}{\lambda} e^{2ikL} \sum_{j=0}^{2N-1} \text{sgn } \phi_j (1+m_j^2)^{1/2} \Delta_j [x_1(j) - x_2(j)]; \quad \Psi = 0, \quad (27a)$$

$$H_1 = e^{i\pi/2} \sum_{j=0}^{2N-1'} \text{sgn } \phi_j (1+m_j^2)^{1/2} e^{2ik\xi_j} \Delta_j \left[\frac{e^{-2ik\xi_j} x_1(j) - e^{-2ik\xi_j} x_2(j)}{\xi_j} \right]; \quad \Psi \neq 0, \quad (27b)$$

where the parameters are defined in Eqs. 13-22. The contributions from the convex and concave edges are given by

$$H_2 = e^{-i\pi/2} \left(1 + \frac{a^2}{L^2}\right)^{1/2} \sum_{j=1, \text{ odd}}^{2N-1'} \Delta'_j \left[\frac{e^{-2ik\xi'_j} L}{\xi'_j} - 1 \right] \quad (28)$$

and

$$H_3 = e^{-i\pi/2} \left(1 + \frac{b^2}{L^2}\right)^{1/2} \sum_{j=0, \text{ even}}^{2N-2} \Delta_j'' \left[\frac{e^{-2ik\xi_j'' L} - 1}{\xi_j''} \right]. \quad (29)$$

The primes on the sums indicate that the totally shadowed edges are excluded from the summation, and ξ_j' and ξ_j'' are given by

$$\xi_j' = \frac{a}{L} \sin \Psi \cos (\theta_{j+1} - \beta) - \cos \Psi, \quad (30)$$

$$\xi_j'' = \frac{b}{L} \sin \Psi \cos (\theta_{j+1} - \beta) - \cos \Psi. \quad (31)$$

The quantities Δ_j' and Δ_j'' are polarization dependent and are given by

$$\Delta_j' = \alpha_j' [\gamma_j' (1 - 2Q_j'^2) + \epsilon_j'] \quad \text{Horizontal Polarization} \quad (32a)$$

$$\Delta_j' = \alpha_j' [\gamma_j' (1 - 2P_j'^2) + \epsilon_j'] \quad \text{Vertical Polarization} \quad (32b)$$

$$\Delta_j' = \alpha_j' [\gamma_j' (1 - P_j'^2 - Q_j'^2) + \epsilon_j'] \quad \text{Circular Polarization} \quad (32c)$$

and

$$\Delta_j'' = \alpha_j'' [\gamma_j'' (1 - 2Q_j''^2) + \epsilon_j''] \quad \text{Horizontal Polarization} \quad (33a)$$

$$\Delta_j'' = \alpha_j'' [\gamma_j'' (1 - 2P_j''^2) + \epsilon_j''] \quad \text{Vertical Polarization} \quad (33b)$$

$$\Delta_j'' = \alpha_j'' [\gamma_j'' (1 - P_j''^2 - Q_j''^2) + \epsilon_j''], \quad \text{Circular Polarization} \quad (33c)$$

where

$$\alpha_j' = \frac{\sin \frac{\pi}{v'}}{v' \sin \delta_j'} \quad , \quad (34a)$$

$$\gamma_j' = \left[\cos \frac{\pi}{v'} - \cos \frac{2\varphi_j'}{v'} \right]^{-1} \quad , \quad (34b)$$

$$\epsilon_j' = \left[\cos \frac{\pi}{v'} - \cos \frac{2\varphi_j'}{v'} \right]^{-1} \quad , \quad (34c)$$

and

$$\alpha_j'' = \frac{\sin \left(\frac{\pi - \bar{\Omega}}{\bar{v}} \right)}{\bar{v} \sin \bar{\delta}_j} \quad , \quad (35a)$$

$$\gamma_j'' = \left[1 + \cos \left(\frac{\pi - \bar{\Omega}}{\bar{v}} \right) \right]^{-1} \quad , \quad (35b)$$

$$\epsilon_j'' = \left[\cos \left(\frac{\pi - \bar{\Omega}}{\bar{v}} \right) + \cos \frac{2\bar{\varphi}_j}{\bar{v}} \right]^{-1} . \quad (35c)$$

The P_j' , Q_j' , P_j'' and Q_j'' are given by

$$P_j' = \left(1 + \frac{L^2}{a^2} \right)^{-1/2} \sin (\theta_{j+1} - \beta) \quad , \quad (36a)$$

$$Q_j' = - \left(1 + \frac{L^2}{a^2} \right)^{-1/2} \left[\cos \Psi \cos (\theta_{j+1} - \beta) + \frac{L}{a} \sin \Psi \right] \quad , \quad (36b)$$

$$P_j'' = \left(1 + \frac{L^2}{a^2} \right)^{-1/2} \sin (\theta_{j+1} - \beta) \quad (37a)$$

and

$$Q_j'' = - \left(1 + \frac{L^2}{b^2}\right)^{-1/2} \left[\cos \Psi \cos (\theta_{j+1} - \beta) + \frac{L}{b} \sin \Psi \right]. \quad (37b)$$

The quantity ν' is given by

$$\nu' = \frac{2\pi - \Omega'}{n} \quad (38)$$

where Ω is the interior angle of the longitudinal convex wedge and may be written as

$$\Omega' = \cos^{-1} \frac{K_1}{K_2}, \quad (39a)$$

$$K_1 = \frac{L^4 (a^2 + b^2 \cos \frac{2\pi}{N} - 2ab \cos \frac{\pi}{N})}{a^4 b^2 \sin^2 \frac{\pi}{N}} + \frac{L^2 (a - b \cos \frac{\pi}{N})^2}{a^2 b^2 \sin^2 \frac{\pi}{N}} - 1 - \frac{2L^2}{a^2} \quad (39b)$$

$$K_2 = \frac{L^4 (a^2 + b^2 - 2ab \cos \frac{\pi}{N})}{a^4 b^2 \sin^2 \frac{\pi}{N}} + \frac{L^2 (b \cos \frac{\pi}{N} - a)^2}{a^2 b^2 \sin^2 \frac{\pi}{N}} + 1 + \frac{2L^2}{a^2} \quad (39c)$$

the interior angle of the longitudinal concave wedge is given by

$$\bar{\Omega} = \cos^{-1} \frac{K_3}{K_4}, \quad (40a)$$

where

$$K_3 = \frac{L^2 (a \cos \frac{\pi}{N} - b)^2}{a^2 b^2 \sin^2 \frac{\pi}{N}} - \frac{L^4 (2ab \cos \frac{\pi}{N} - a^2 \cos \frac{2\pi}{N} - b^2)}{a^2 b^4 \sin^2 \frac{\pi}{N}} - 1 - \frac{2L^2}{b^2} \quad (40b)$$

and

$$K_4 = \frac{L^4 (a^2 + b^2 - 2ab \cos \frac{\pi}{N})}{a^2 b^2 \sin^2 \frac{\pi}{N}} + \frac{L^2 (a \cos \frac{\pi}{N} - b)^2}{a^2 b^2 \sin^2 \frac{\pi}{N}} + 1 + \frac{2L^2}{b^2} \quad (40c)$$

The angles δ'_j and $\bar{\delta}_j$ are given by

$$\delta'_j = \cos^{-1} \left\{ \left(1 + \frac{L^2}{a^2} \right)^{-1/2} \left(\frac{L \cos \Psi}{a} - \cos (\theta_{j+1} - \beta) \sin \Psi \right) \right\} \quad (41a)$$

and

$$\bar{\delta}_j = \cos^{-1} \left\{ \left(1 + \frac{L^2}{b^2} \right)^{-1/2} \left(\frac{L}{b} \cos \Psi - \cos (\theta_{j+1} - \beta) \sin \Psi \right) \right\} \quad (41b)$$

while the angles φ'_j and $\bar{\varphi}_j$ may be expressed as

$$\cos \varphi'_j = -K_2^{-1/2} (\sin \delta_j)^{-1} \left[\frac{L^2}{a^2 b \sin \frac{\pi}{N}} \left\{ a \cos (\theta_{j+1} - \beta) \sin \Psi - b \cos (\theta_{j+2} - \beta) \sin \Psi + \right. \right. \\ \left. \left. \frac{a}{L} (a - b \cos \frac{\pi}{N}) \cos \Psi \right\} + \sin \Psi \sin (\theta_{j+1} - \beta) \right] \quad (42)$$

$$\cos \bar{\varphi}_j = -K_4^{-1/2} (\sin \bar{\delta}_j)^{-1} \left[\frac{L^2}{ab^2 \sin \frac{\pi}{N}} \left\{ b \cos (\theta_{j+1} - \beta) \sin \Psi - a \cos (\theta_{j+2} - \beta) \sin \Psi - \right. \right. \\ \left. \left. \frac{b}{L} (a \cos \frac{\pi}{N} - b) \cos \Psi \right\} + \sin \Psi \sin (\theta_{j+1} - \beta) \right] \quad (43)$$

It should be noted that the wedge diffraction coefficients do not provide an adequate representation of the scattered fields when the direction of incidence approaches the tangent to the edge (i.e., δ'_j or $\overline{\delta}_j \approx 0^\circ$). This condition occurs for near nose-on incidence on the pyramid. It has been seen, however, that the contribution of the rear edges is sufficient to describe the small-angle scattering characteristics so that the contribution from the longitudinal edges need not be included for aspect angles smaller than the pyramid half-angle.

The wedge diffraction coefficients used in this work are obtained from the asymptotic expansions of the diffracted backscattered field for incidence angles away from the geometrical optics boundary (i.e., ϕ'_j or $\overline{\phi}_j \approx \frac{\pi}{2}$). Unfortunately, the incident field approaches this boundary on the convex edges (i.e., $\phi'_j \approx \frac{\pi}{2}$) for several cases treated in this report. In most cases, however, the concave edges are dominating the return by the time this condition is reached and so the best approximation to the large angle ($8^\circ < \Psi \leq 30^\circ$) scattering of the target was obtained by considering the contributions to the return from the rear and concave edges only. The resultant form for the RCS of the pyramid in the aspect interval $8^\circ < \Psi \leq 30^\circ$ may be written as

$$\sigma = \frac{\lambda^2}{16\pi^3} \left| H_1 + H_3 \right|^2. \quad (44)$$

The shadow boundaries were accounted for in the calculation of H_3 , while the shadowing of the rear edges was considered to be negligible on the basis of the results of the previous section.

The theoretical curves shown in the following results are obtained by using the contribution from the rear edges alone (i.e., Eq. 12) for aspect angles smaller than the pyramid half-angle and the contributions from the rear and longitudinal

concave edges (i.e., Eq. 44) for angles greater than the pyramid half-angle. The calculations for the three-noded pyramid only are shown here as they are representative of the results obtained by using Eq. (44) for large aspect angles.

In many cases the inclusion of the concave edges in the scattering description resulted in the prediction of the lobe structure seen at larger aspect angles in the data. In some of these instances, however, the predicted peaks and nulls of the lobes were shifted from their observed positions. An example of this is seen in the 4.03 GHz circularly polarized return from the target in a 0° roll orientation shown in Fig. 18a. The predicted peaks and nulls are shifted by 8° and the predicted RCS value at the peak is a few dB high. Fig. 18b indicates that, in an unsymmetrical case, the predicted return for positive values of Ψ are in reasonable agreement with the measured results. At negative aspect angles, however, the sharp null seen in the measurements at -19° is shifted to -25° in the predictions which also display a 5 dB increase preceeding the null that is absent from the measurements. Figs. 19a and 19b show the horizontally polarized returns at the same frequency for roll angles of 0° and 60° . The slight peaking of the RCS near 12° and the sharp null that follows is accounted for by the theory, although these features are shifted by 5° .

The use of Eq. (44) did not improve the vertically polarized returns as seen in Figs. 20a and 20b. At 3.00 GHz, the horizontally polarized predictions are quite close to the measurements as seen in Figs. 21a and 21b; although the vertically polarized results do not show a great deal of improvement as indicated by Figs. 22a and 22b.

The 1.00 GHz results are not included, as the utilization of Eq. (44) did not greatly affect the general shape of the predicted results. They did lead, however, to a slight increase in the RCS level; bringing the predictions closer to the measured values.

V. CONCLUSIONS

Ross's modification of GTD has been presented and seen to yield reasonable results when applied to a complex body such as the N-noded pyramid. Ross utilized this technique in order to improve the caustic correction that was necessary to apply to the original results of Keller. The Keller formulation may be obtained from this modification by evaluating Eq. (1) by stationary phase.

The rear edges were treated by extending the integration around the entire rim discontinuity so that the influence of the cusps on the backscattered field is contained implicitly in this formulation. Although this treatment of the cusps is not rigorous, as there is no canonical solution to represent their scattering contribution, it provides adequate predictions in most cases for the aspect intervals of interest.

The results of Section III indicate that, except for the cases listed in Table 2, the contributions of the rear edges alone provide a good approximation to the measured RCS for a minimum aspect interval of 12° ; which is 1.5 times the pyramid half-angle and for a range of frequencies such that $1.9 \leq ka \leq 7.6$. The rear edge predictions for the cases listed in Table 2 were valid only out to 8° , the pyramid half-angle. These calculations were performed, assuming the rear edges remained completely illuminated throughout the entire aspect interval, although a geometrical prescription of the shadowing indicates that shadowing of the rear edges by neighboring edges is initiated at very small aspect angles. This discrepancy can be explained, as mentioned earlier, by the fact that the actual shadow boundary is not a sharply defined discontinuity because of the finite wavelength of the incident radiation.

The predictions for the vertically polarized radiation were, in general, the least accurate. This weakness of GTD might be attributed to the excitation of modes on the structure which are not accounted for in this unsophisticated geometrical theory.

In order to improve the RCS predictions obtained by a consideration of only the rear edges, an attempt was made to incorporate the return from the longitudinal

edges into the total RCS predictions. The effects of this modification, presented in Section IV, were somewhat inconclusive. It was found that, in some cases, the combination of the return from the rear and concave edges led to results that were in very good agreement with the measurements. In other cases, such as the vertically polarized returns, the predictions remained poor at the larger aspect angles. The return from the convex edges could not be included in this work because, in each case, there was an aspect angle interval in which the incident wave approached the geometrical optics boundary of at least one of the edges. This deficiency can be corrected by the substitution of the appropriate representation of the scattered fields on the boundary.

The only obvious modification to the present work to be suggested is the substitution of the correct diffraction coefficient for the case of the incident radiation being in the vicinity of the geometrical optics boundary. This improvement would permit the contribution of the convex edges to be included and could lead to an improvement in the theoretical predictions at aspect angles greater than the half-angle. If this change should not make an appreciable difference, it appears that the next step would be to obtain a complete numerical solution of the wave equation for the pyramid geometry.

REFERENCES

1. R. A. Ross, "Small-Angle Scattering by a Finite Cone," IEEE Trans. Antennas Propag. AP-17, 241-242 (1969).
2. J. B. Keller, "Geometrical Theory of Diffraction," J. Opt. Sci. Am. 52, 116-130 (1962).
3. J. B. Keller, "Backscattering from a Finite Cone," IRE Trans. Antennas Propag. AP-8, 175-182 (1960).
4. D. M. Raybin, "Radar Cross Section of Spherical Shell Sections," IEEE Trans. Antennas Propag. AP-13, 754-759 (1965).
5. W. H. Schoendorf, "Small-Angle Scattering from an Involute Pyramid," IEEE Trans. Antennas Propag. AP-20, 794-796 (1972).

APPENDIX I

Shadow Boundaries on the Rear and the Longitudinal Edges

The shadow boundaries on the rear and the longitudinal edges are derived in this appendix. It is assumed that the wavelength of the incident radiation is small enough to invoke a geometrical optics formulation of these boundaries.

Since the treatment of the longitudinal edges follows from that of the rear edges, the latter are treated first.

In order for the j^{th} rear edge to receive any illumination, it is necessary that $\hat{k} \cdot \hat{n}_j < 0$, where \hat{n}_j is the unit outward normal from the j^{th} slant surface. This criterion may be written as

$$\frac{L}{K_2} [a \sin(\beta - \theta_{j+1}) + b \sin(\theta_j - \beta)] - \cos \Psi < 0, j \text{ odd} \quad (\text{A-1})$$

$$\frac{L}{K_2} [a \sin(\theta_j - \beta) + b \sin(\beta - \theta_{j+1})] - \cos \Psi < 0, j \text{ even} \quad (\text{A-2})$$

The edges that satisfy these equations must now be investigated in order to determine if they are shadowed by a neighboring cusp. It is obvious from Fig. 1 that the j^{th} edge can only be shadowed by the cusp made up of the $j+1$, $j+2$ edges for j even, and the $j-2$, $j-1$ edges for j odd. The shadow boundary cast by each cusp is determined by considering the intersection of the plane containing \hat{k} and the line formed by the intersection of two adjacent slant surfaces, with the base of the

target. If the point at which this plane intersects the base falls within the limits of the j^{th} edge, this edge will be partially shadowed by the cusp of interest. If this point is exterior to the pyramid, the edge is completely shadowed by the cusp; and if the point lies in the interior of the pyramid, the edge is completely illuminated.

The x coordinate of this shadow point cast by the $j, j+1$ cusp on the $j-1$ edge (i. e., even edge) is given by

$$x_s(j-1) = \frac{N_1}{D_1} , \quad (\text{A-3})$$

where

$$\begin{aligned} N_1 = & L \sin \Psi \sin (\beta - \theta_{j+1}) [a \cos \theta_{j-1} - b \cos \theta_j] \\ & + ab \cos \Psi \sin \frac{\pi}{N} \cos \theta_{j+1} + Lb \sin \Psi \cos \beta \sin \frac{\pi}{N} \end{aligned} \quad (\text{A-4})$$

and

$$\begin{aligned} D_1 = & a \cos \Psi \sin \frac{2\pi}{N} + L \sin \Psi \sin (\beta - \theta_{j-1}) \\ & - b \cos \Psi \sin \frac{\pi}{N} + \frac{LB}{a} \sin \Psi \sin (\theta_j - \beta) \end{aligned} \quad (\text{A-5})$$

while the shadow point cast on the $j+2$ edge (i. e., odd edge) is given by

$$x_s(j+2) = \frac{N_2}{D_2} , \quad (\text{A-6})$$

where

$$\begin{aligned}
 N_2 = & L \sin \Psi \sin (\beta - \theta_{j+1}) [b \cos \theta_{j+2} - a \cos \theta_{j+3}] \\
 & + ab \cos \Psi \sin \frac{\pi}{N} \cos \theta_{j+1} + Lb \sin \Psi \cos \beta \sin \frac{\pi}{N}
 \end{aligned}
 \tag{A-7}$$

and

$$\begin{aligned}
 D_2 = & a \cos \Psi \sin \frac{2\pi}{N} - L \sin \Psi \sin (\beta - \theta_{j+3}) \\
 & - b \cos \Psi \sin \frac{\pi}{N} + \frac{Lb}{a} \sin \Psi \sin (\beta - \theta_{j+2})
 \end{aligned}
 \tag{A-8}$$

The evaluation of $x_1(j)$ and $x_2(j)$ is described in Table A-1.

The shadowing of the longitudinal edges may be obtained from the results of Table A-1. The j^{th} longitudinal edge is the intersection of the j^{th} and $j+1$ rear edge. The edge is associated with a concave wedge when j is even and a convex wedge when j is odd. They are either totally illuminated or shadowed, depending on the status of the j^{th} or $j+1$ rear edges. When j is even, the j^{th} longitudinal edge is illuminated if either the j^{th} or $j+1$ rear edge is totally illuminated. When j is odd, the j^{th} longitudinal edge is illuminated if the j^{th} or $j+1$ rear edge is partially or totally illuminated.

TABLE A-1
ILLUMINATION BOUNDARIES

Illumination Boundaries on j-1 Edge			
Condition	Criterion	Result	$\frac{x_1}{x_2}$
$\cos \theta_{j-1} < 0$	$x_s < a \cos \theta_{j-1}$	Edge completely shadowed	---
$\cos \theta_{j-1} < 0$	$x_s > b \cos \theta_j$	Edge completely illuminated	$a \cos \theta_{j-1}$
$\cos \theta_{j-1} > 0$	$x_s > a \cos \theta_{j-1}$	Edge completely shadowed	---
$\cos \theta_{j-1} > 0$	$x_s < b \cos \theta_j$	Edge completely illuminated	$a \cos \theta_{j-1}$
$\theta_{j-1} = \frac{\pi}{2}$	$x_s \geq 0$	Edge completely shadowed	---
$\theta_{j-1} = \frac{\pi}{2}$	$x_s \leq b \cos \theta_j$	Edge completely illuminated	$a \cos \theta_{j-1}$
$\theta_{j-1} = \frac{3\pi}{2}$	$x_s \leq 0$	Edge completely shadowed	---
$\theta_{j-1} = \frac{3\pi}{2}$	$x_s \geq b \cos \theta_j$	Edge completely illuminated	$a \cos \theta_{j-1}$
If neither the completely illuminated nor shadowed criteria are met, the edge is partially illuminated			
x_s			$a \cos \theta_{j-1}$
Illumination Boundaries on j + 2 Edge			
Condition	Criterion	Result	$\frac{x_1}{x_2}$
$\cos \theta_{j+3} < 0$	$x_s < a \cos \theta_{j+3}$	Edge completely shadowed	---
$\cos \theta_{j+3} < 0$	$x_s > b \cos \theta_{j+2}$	Edge completely illuminated	$b \cos \theta_{j+2}$
$\cos \theta_{j+3} > 0$	$x_s > a \cos \theta_{j+3}$	Edge completely shadowed	---
$\cos \theta_{j+3} > 0$	$x_s < b \cos \theta_{j+2}$	Edge completely illuminated	$b \cos \theta_{j+2}$
$\theta_{j+3} = \pi/2$	$x_s \leq 0$	Edge completely shadowed	---
$\theta_{j+3} = \pi/2$	$x_s \geq b \cos \theta_{j+2}$	Edge completely illuminated	$b \cos \theta_{j+2}$
$\theta_{j+3} = 3\pi/2$	$x_s \geq 0$	Edge completely shadowed	---
$\theta_{j+3} = 3\pi/2$	$x_s \leq b \cos \theta_{j+2}$	Edge completely illuminated	$b \cos \theta_{j+2}$
If neither the completely illuminated nor shadowed criteria are met, the edge is partially illuminated			
			x_s

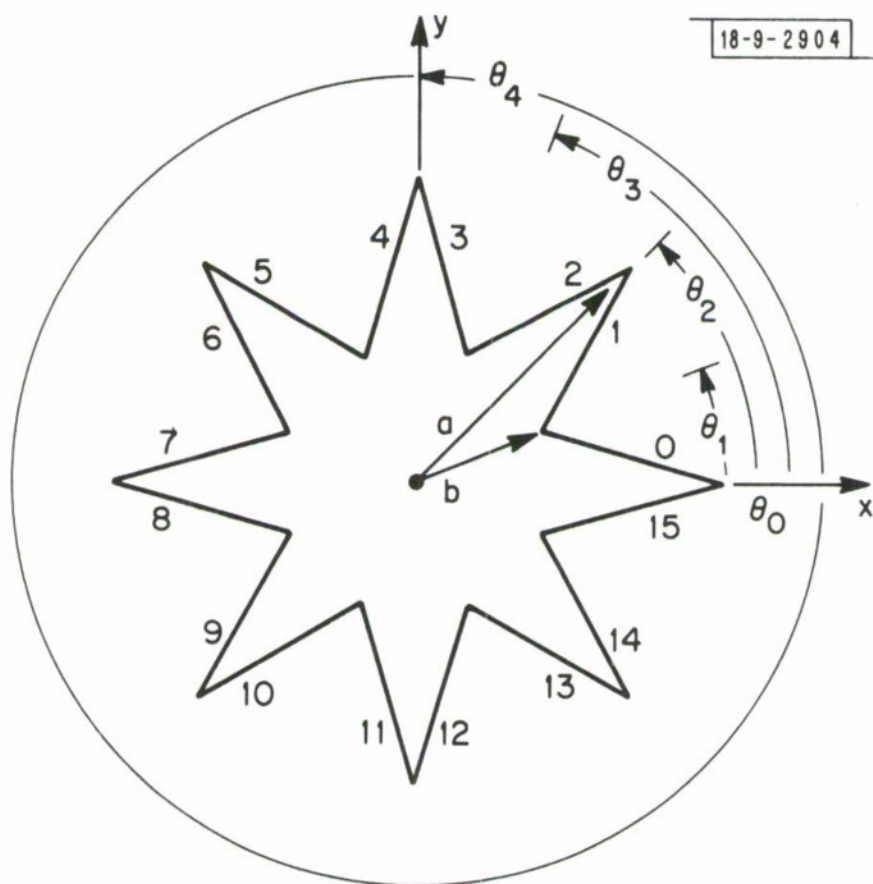


Fig. 1. Pyramid base.

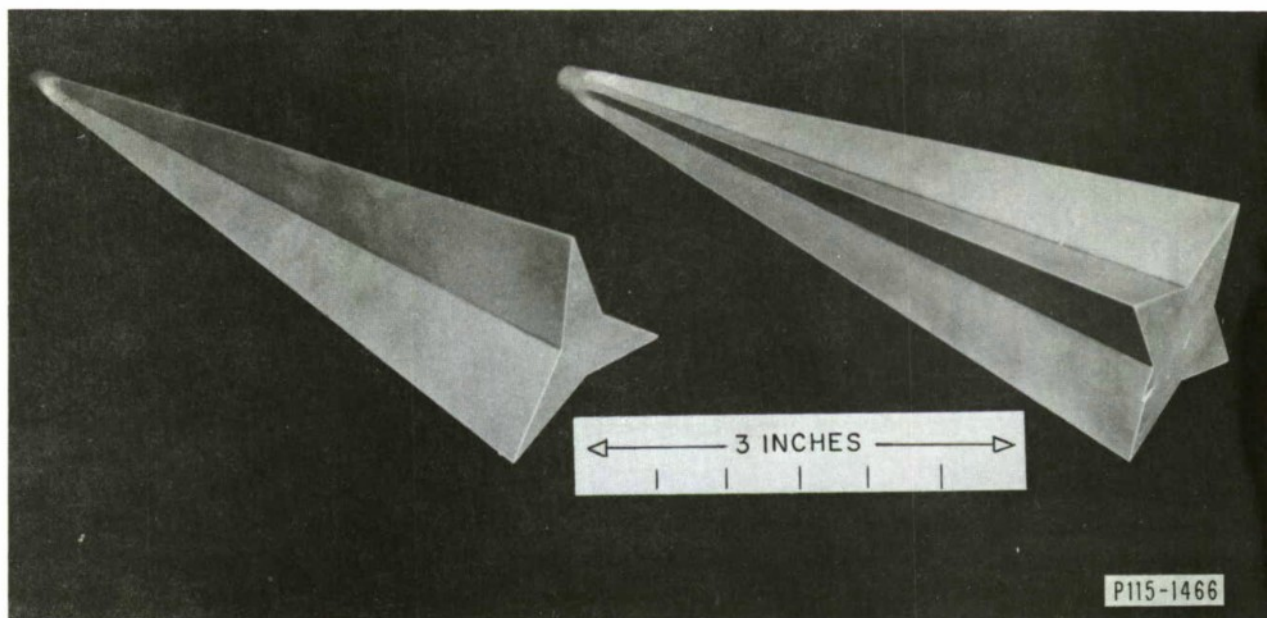


Fig. 2. Three- and four-noded pyramids.

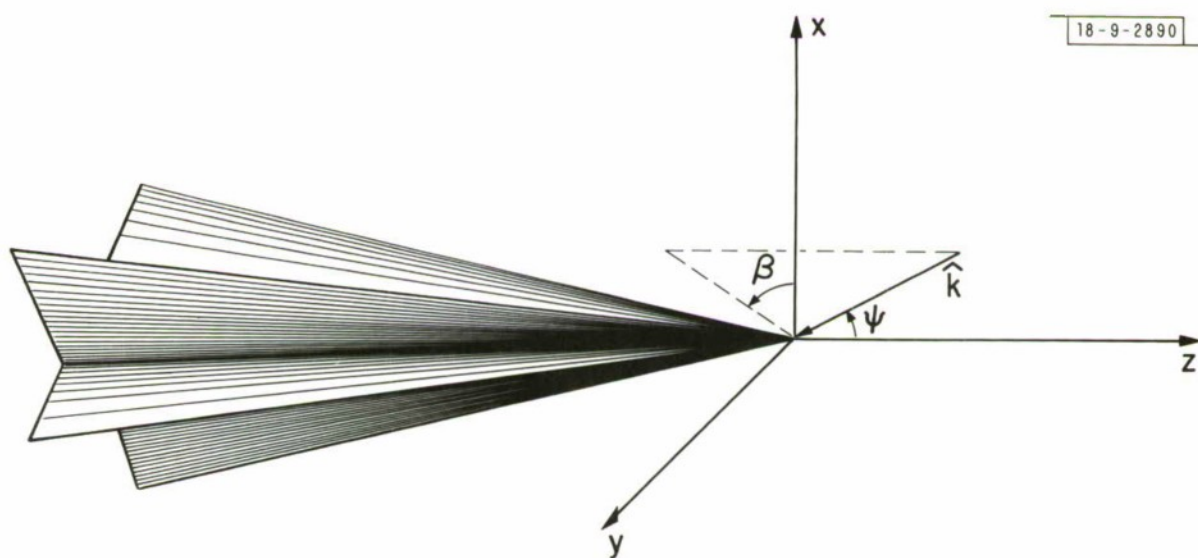


Fig. 3. Scattering geometry.

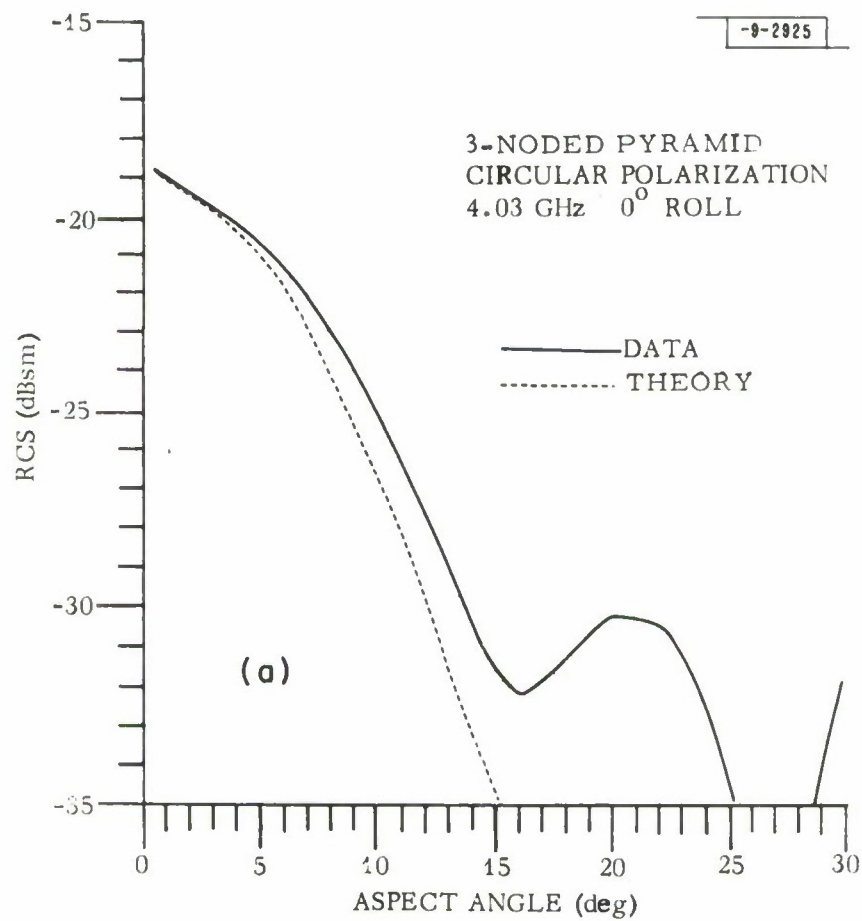


Fig. 4. Circularly polarized radar cross section of three-noded pyramid at 4.03 GHz.

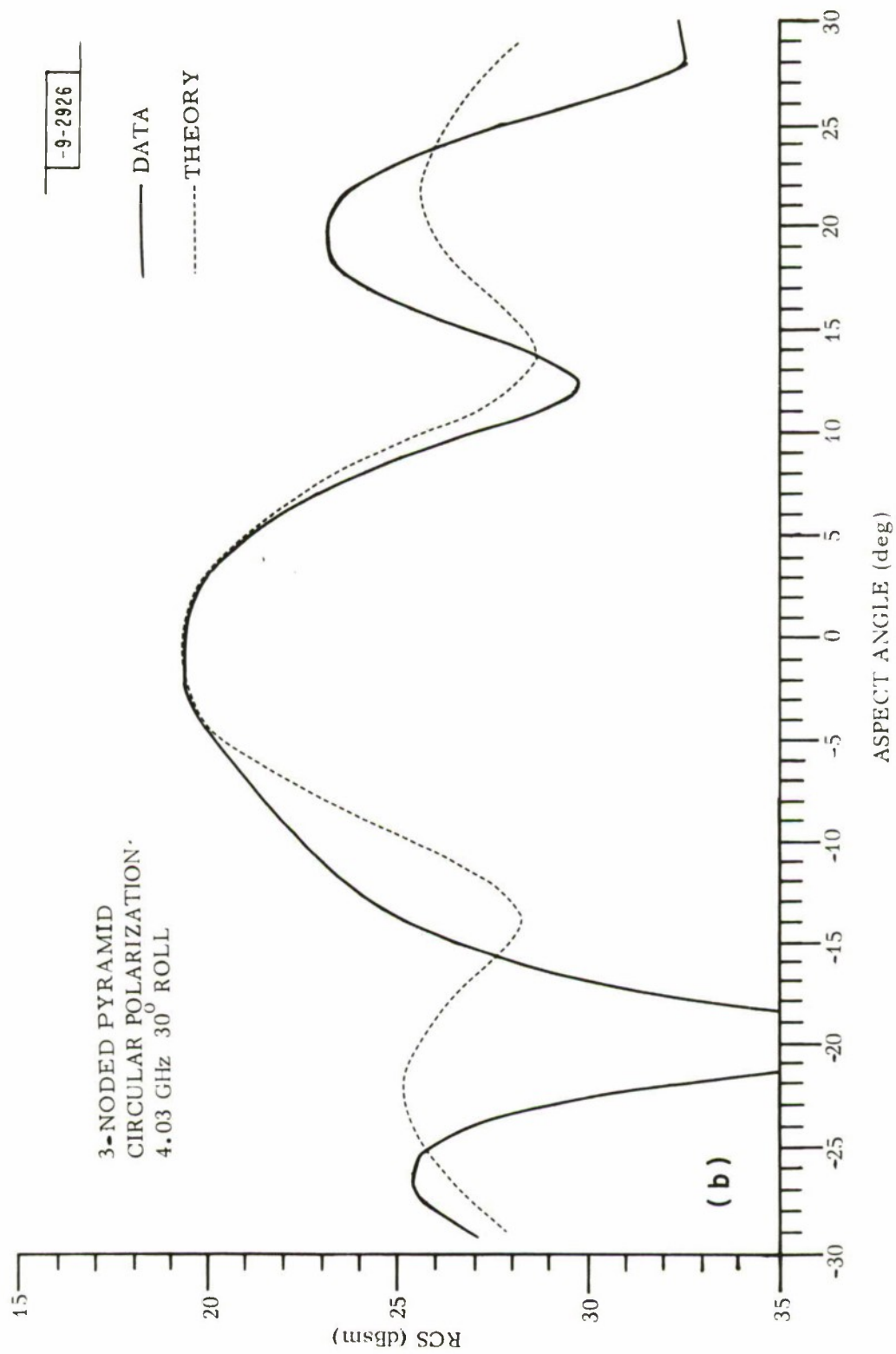


Fig. 4. Continued.

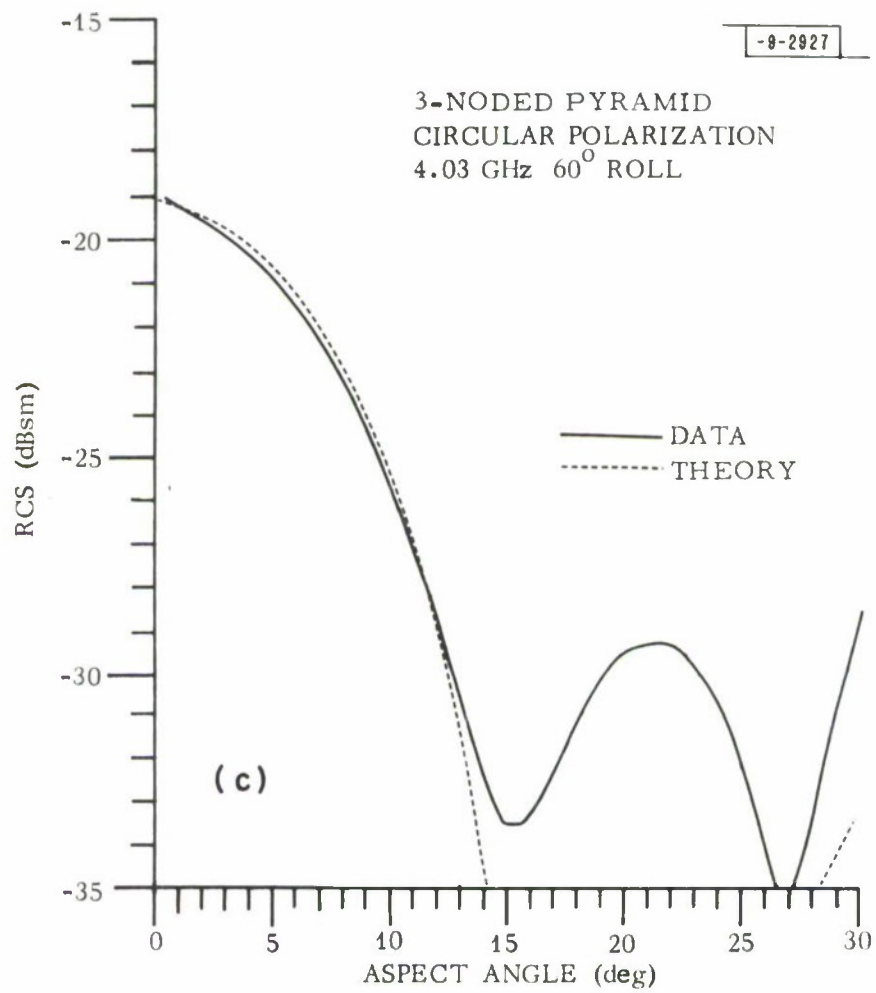


Fig. 4. Continued.

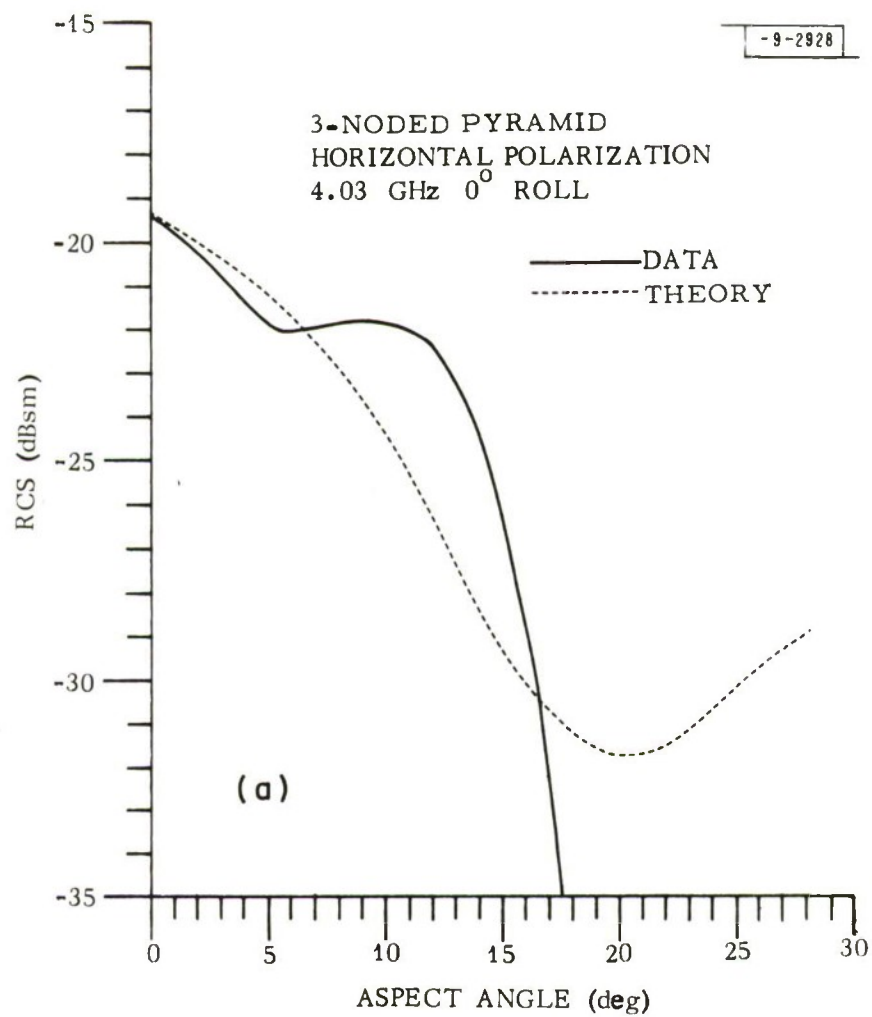


Fig. 5. Horizontally polarized radar cross section of three-noded pyramid at 4.03 GHz.

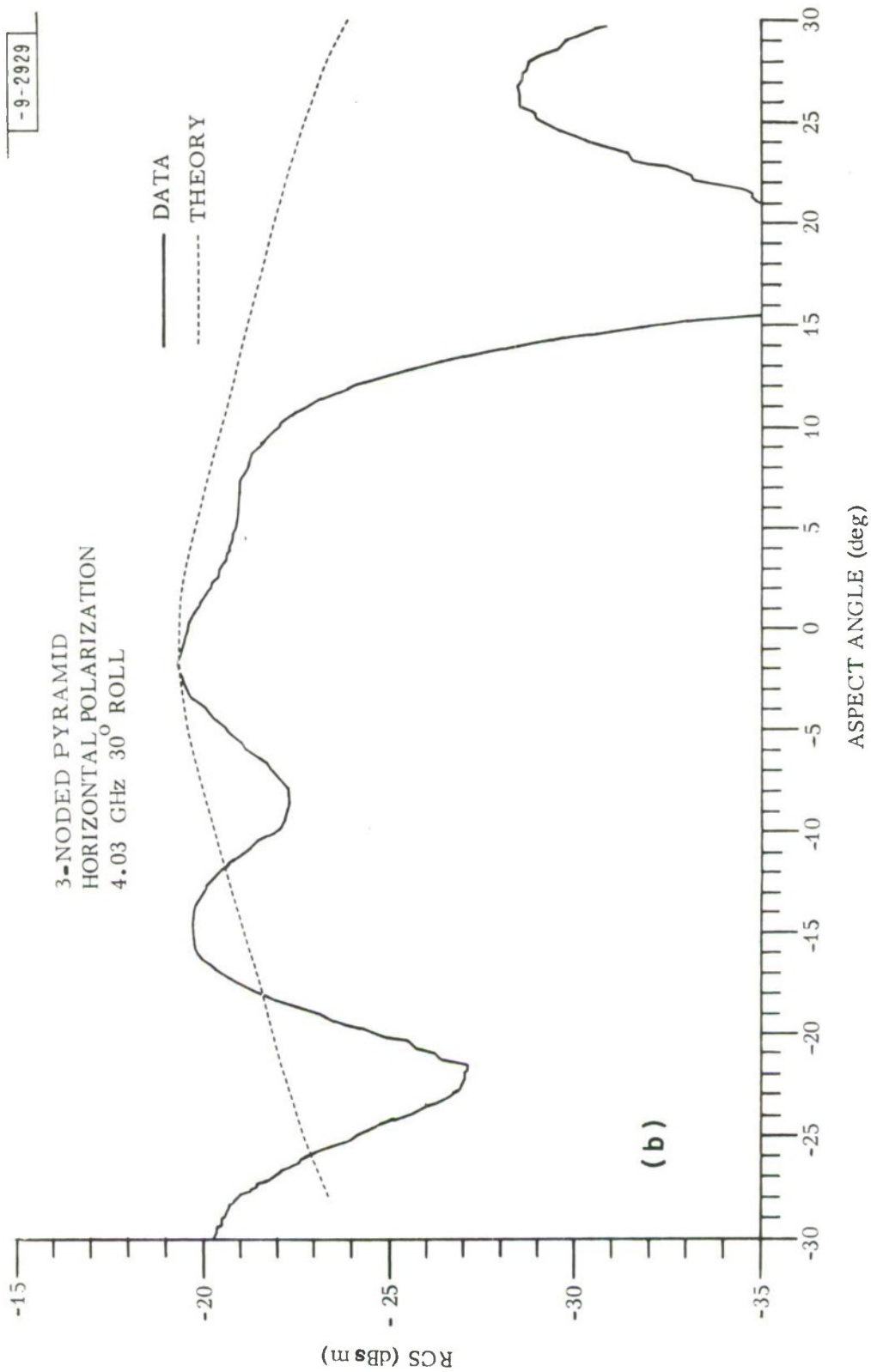


Fig. 5. Continued.

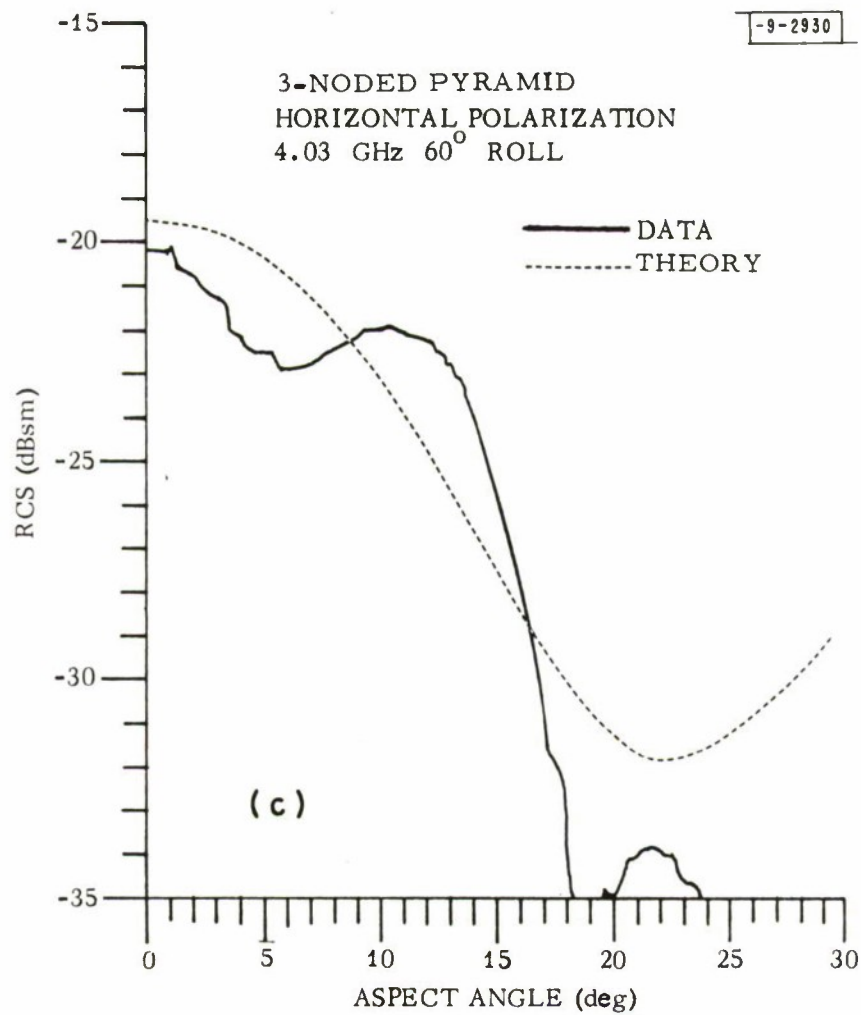


Fig. 5. Continued.

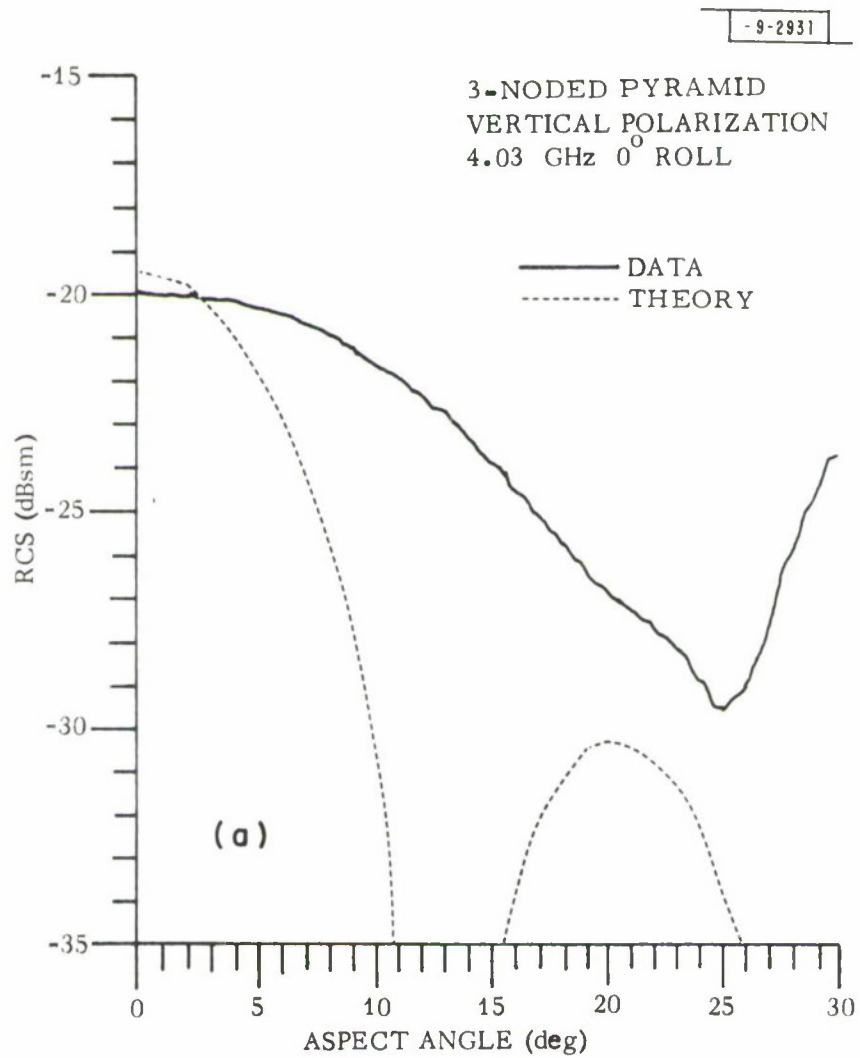


Fig. 6. Vertically polarized radar cross section of three-noded pyramid at 4.03 GHz.

-9-2932

3-NODED PYRAMID
VERTICAL POLARIZATION
4.03 GHz 30° ROLL

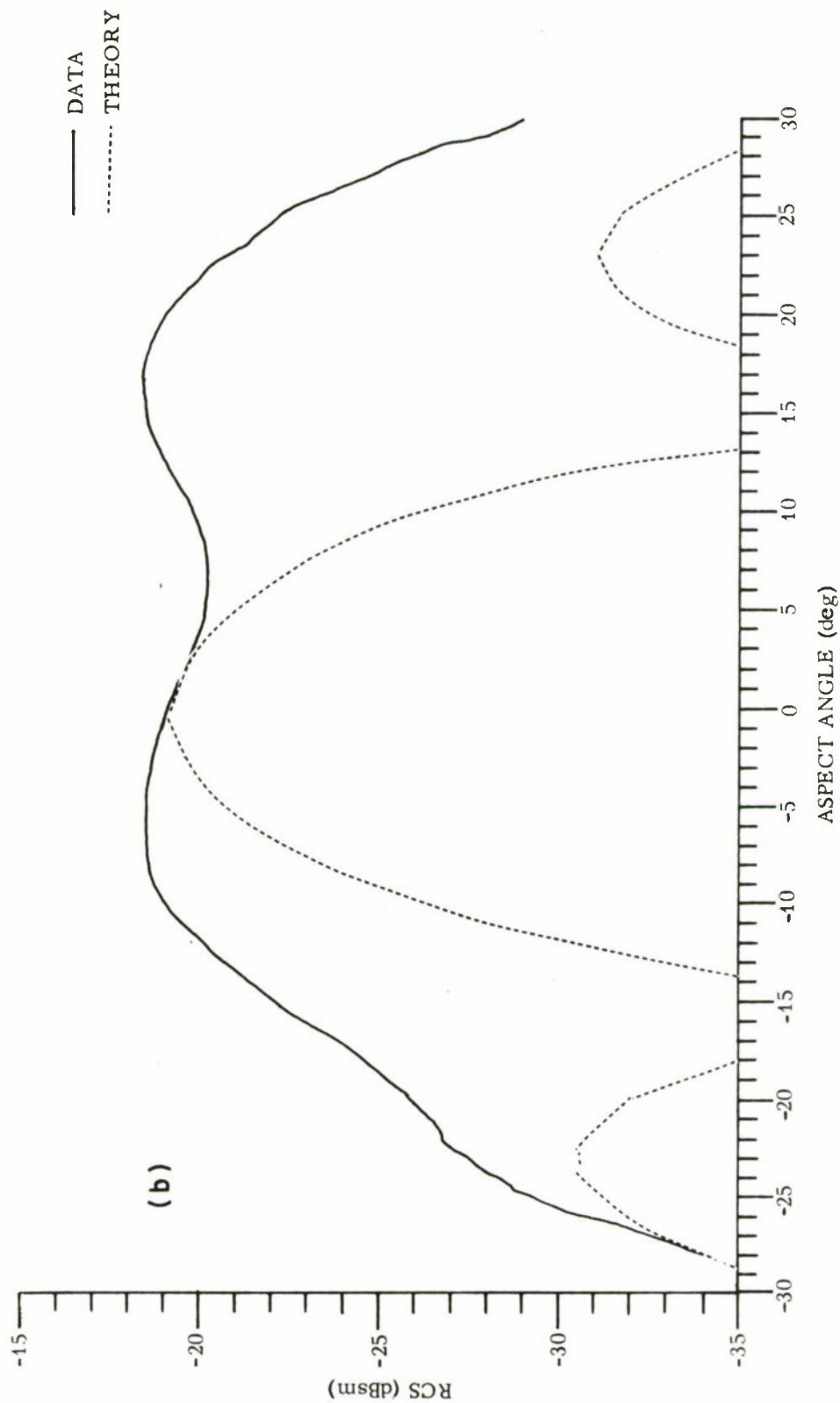


Fig. 6. Continued.

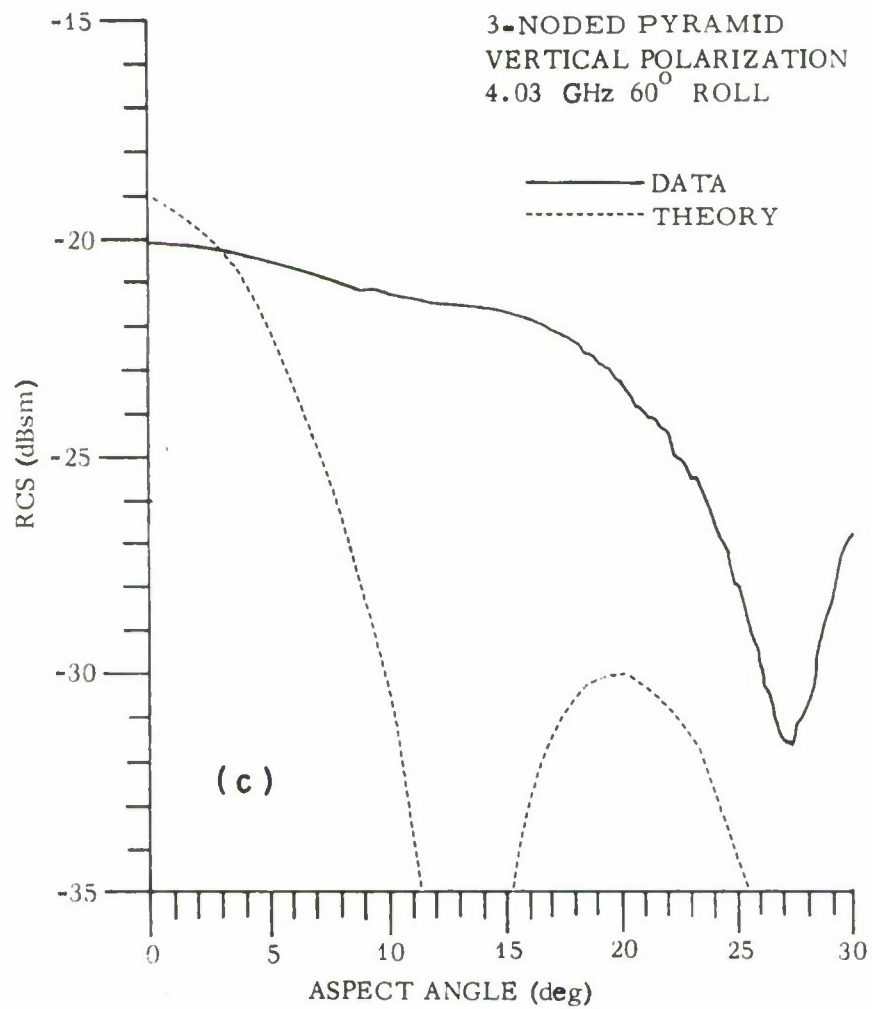


Fig. 6. Continued.

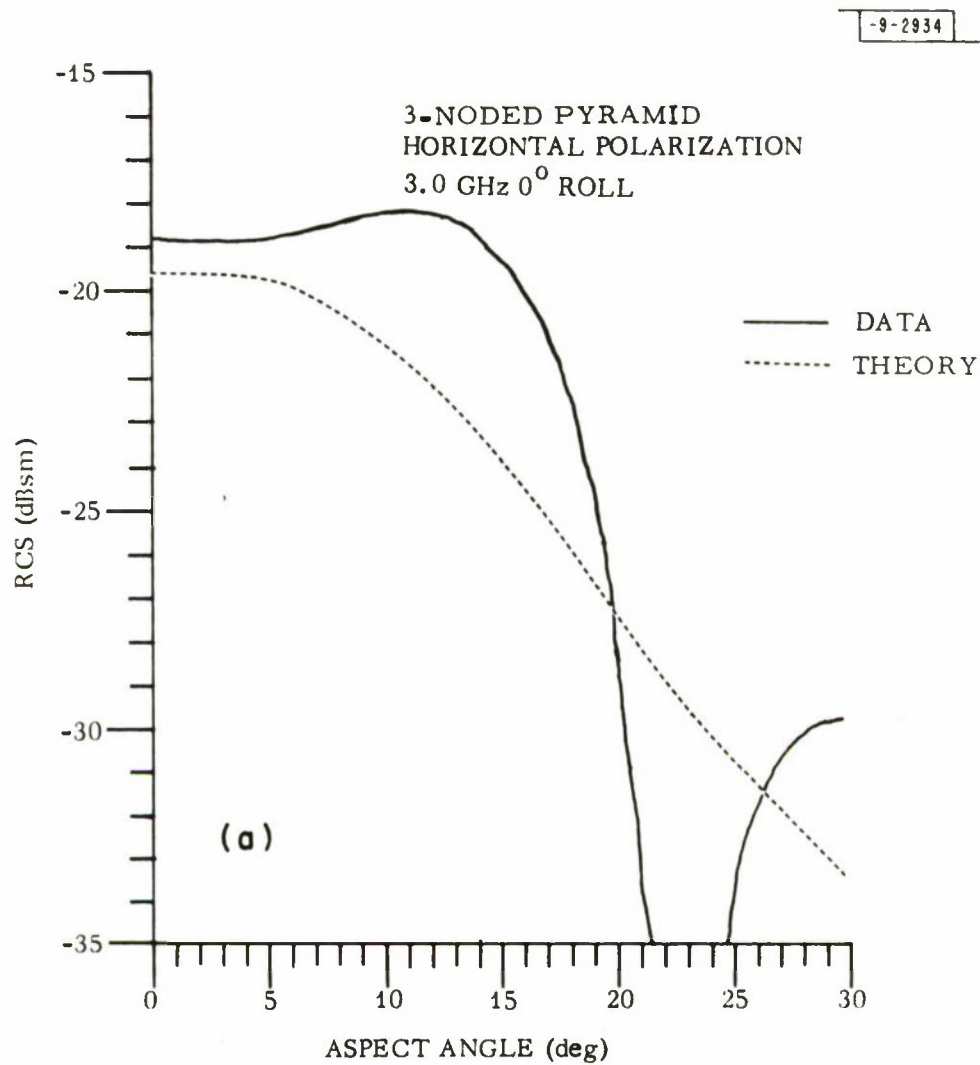


Fig. 7. Horizontally polarized radar cross section of three-noded pyramid at 3.0 GHz.

- 9 - 2935

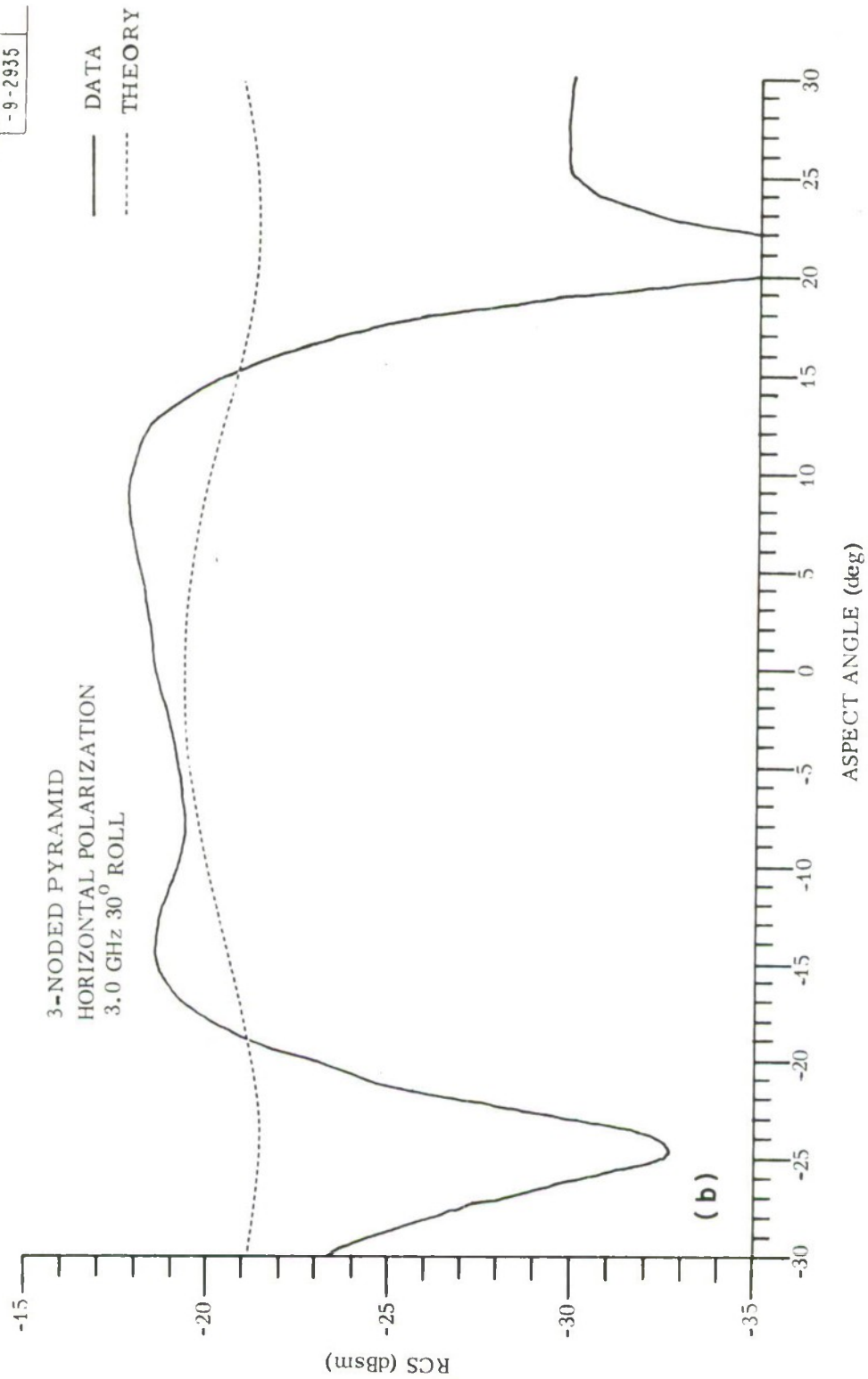


Fig. 7. Continued.

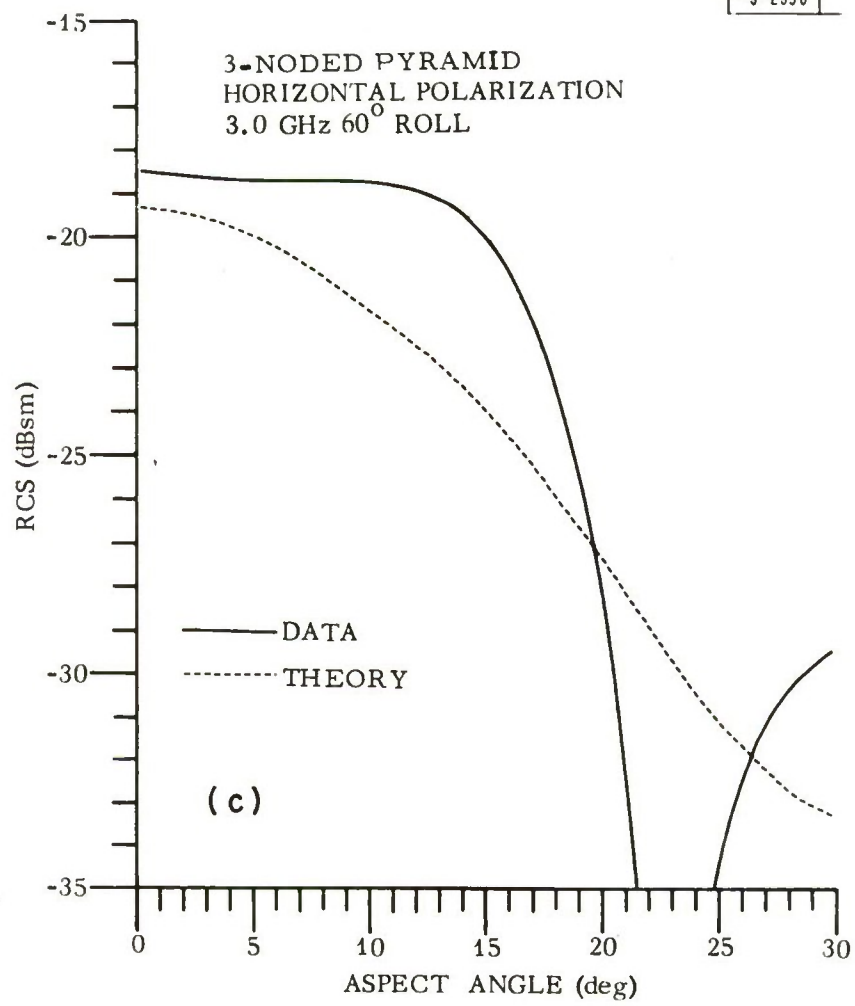


Fig. 7. Continued.

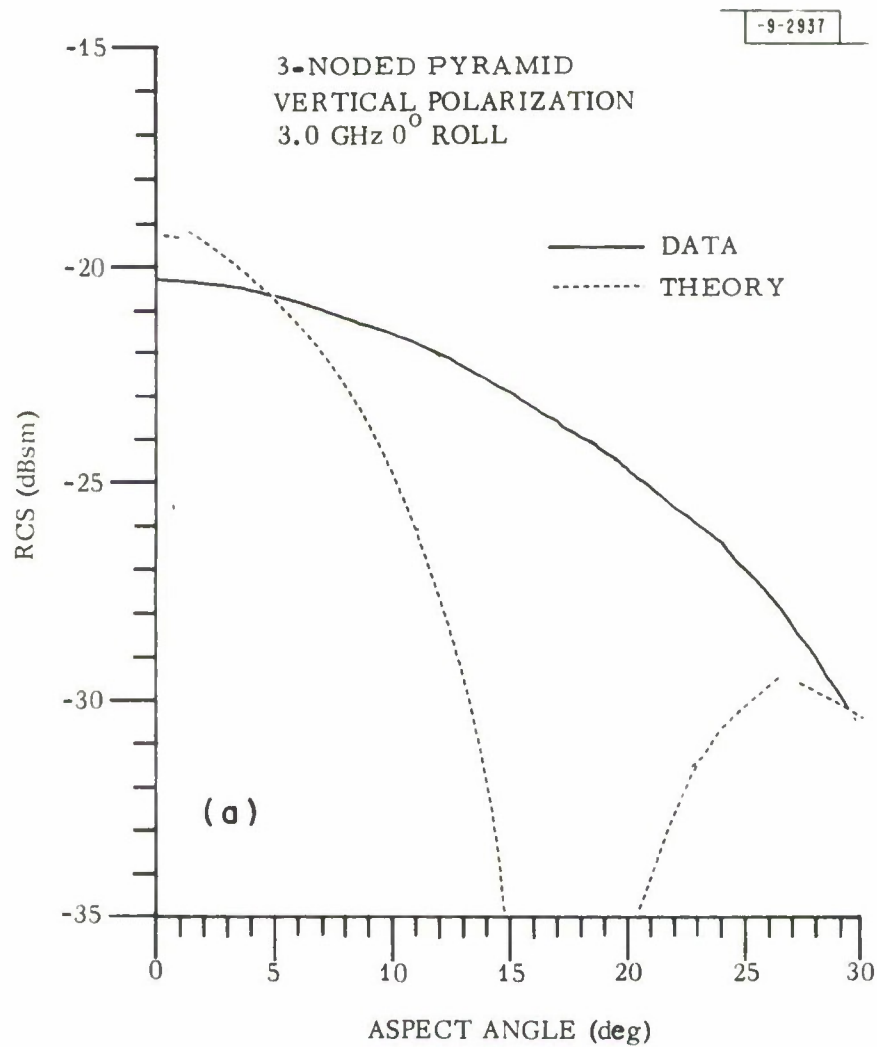


Fig. 8. Vertically polarized radar cross section of three-noded pyramid at 3.0 GHz.

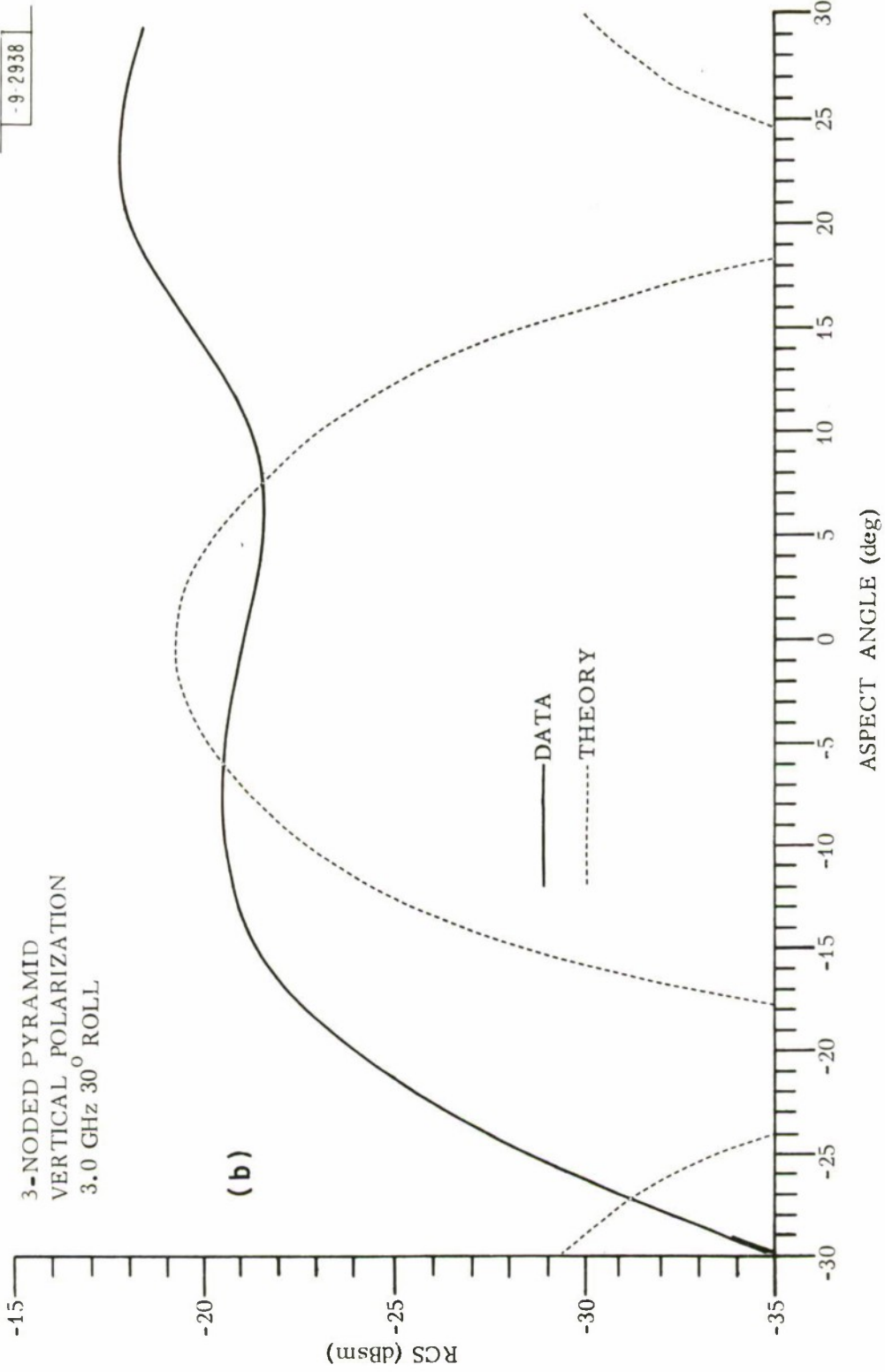


Fig. 8. Continued.

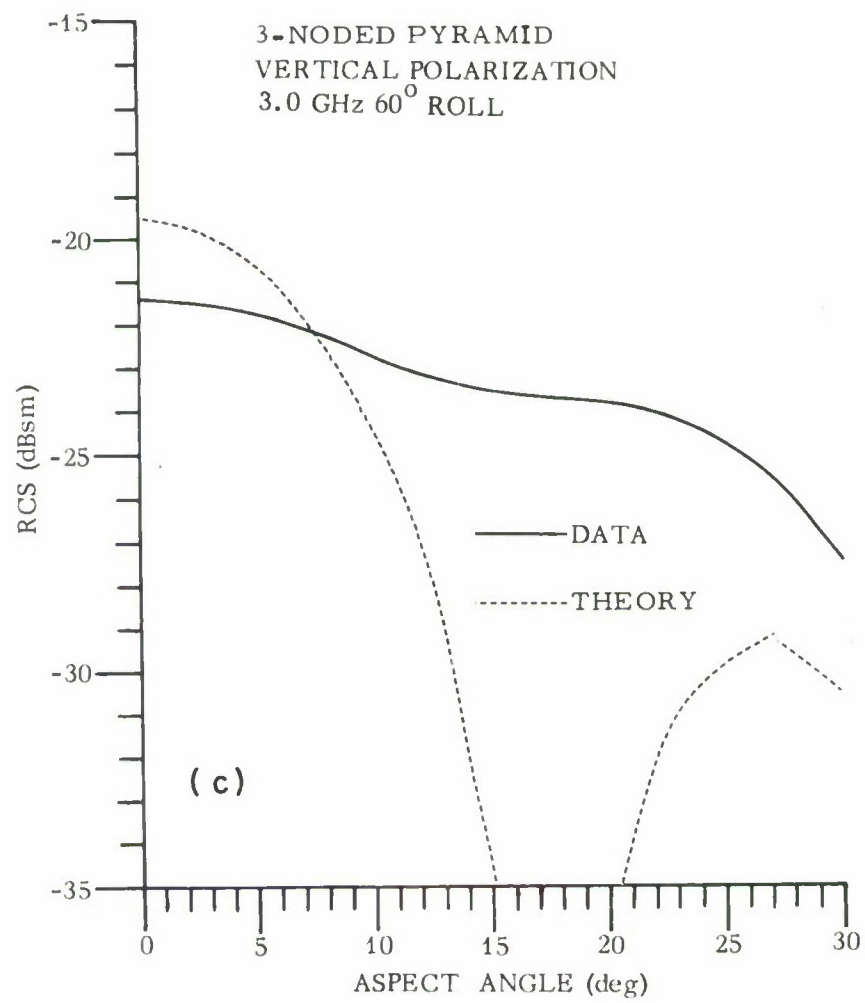


Fig. 8. Continued.

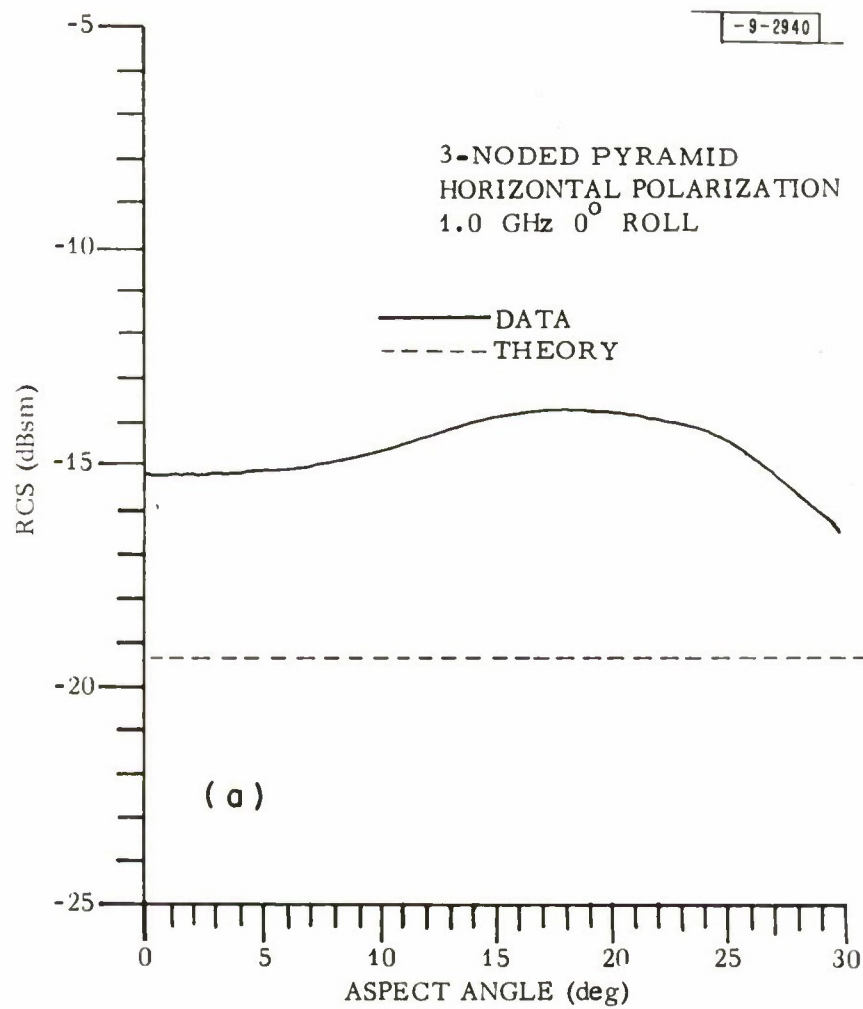


Fig. 9. Horizontally polarized radar cross section of three-noded pyramid at 1.0 GHz.

3-NODED PYRAMID
HORIZONTAL POLARIZATION
1.0 GHz 30° ROLL

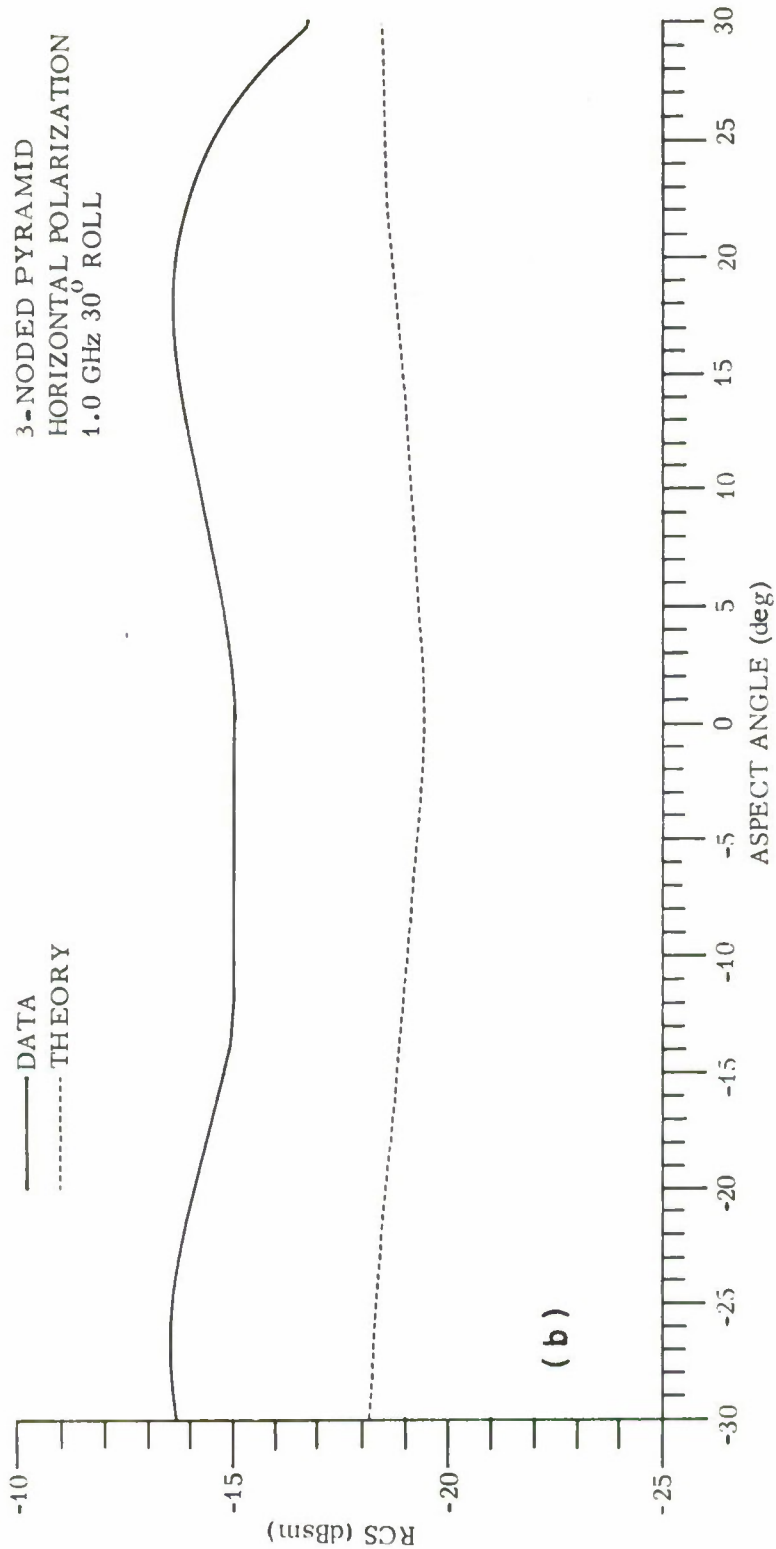


Fig. 9. Continued.

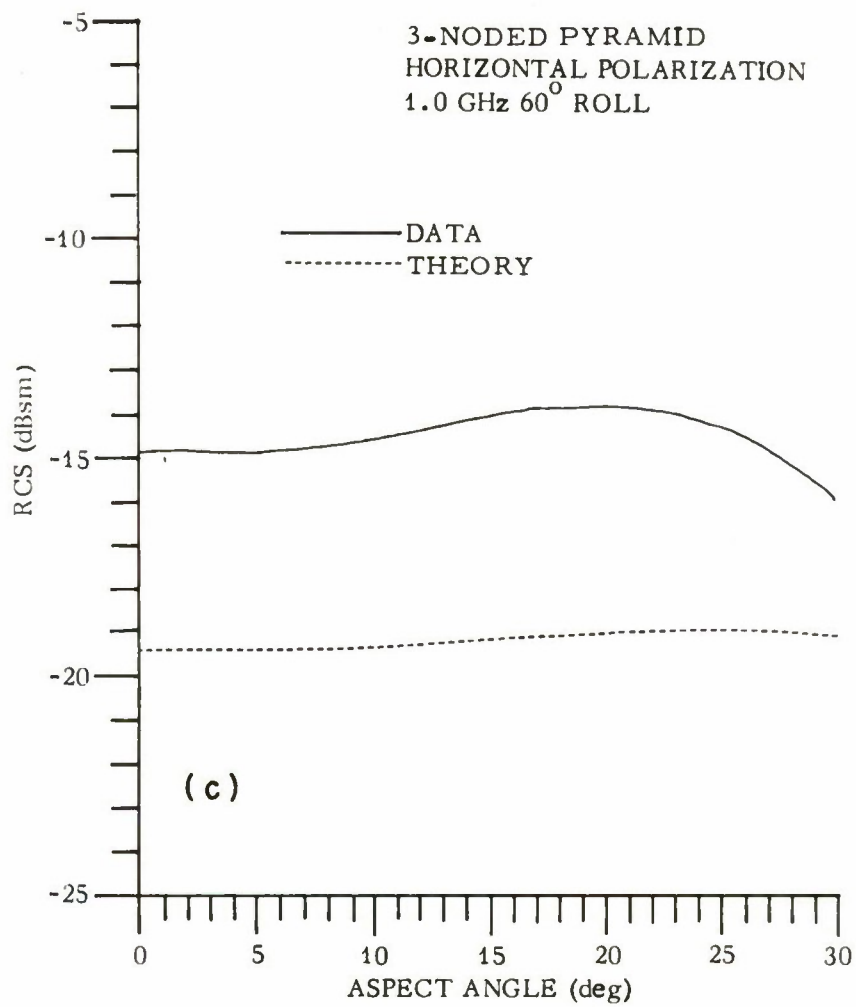


Fig. 9. Continued.

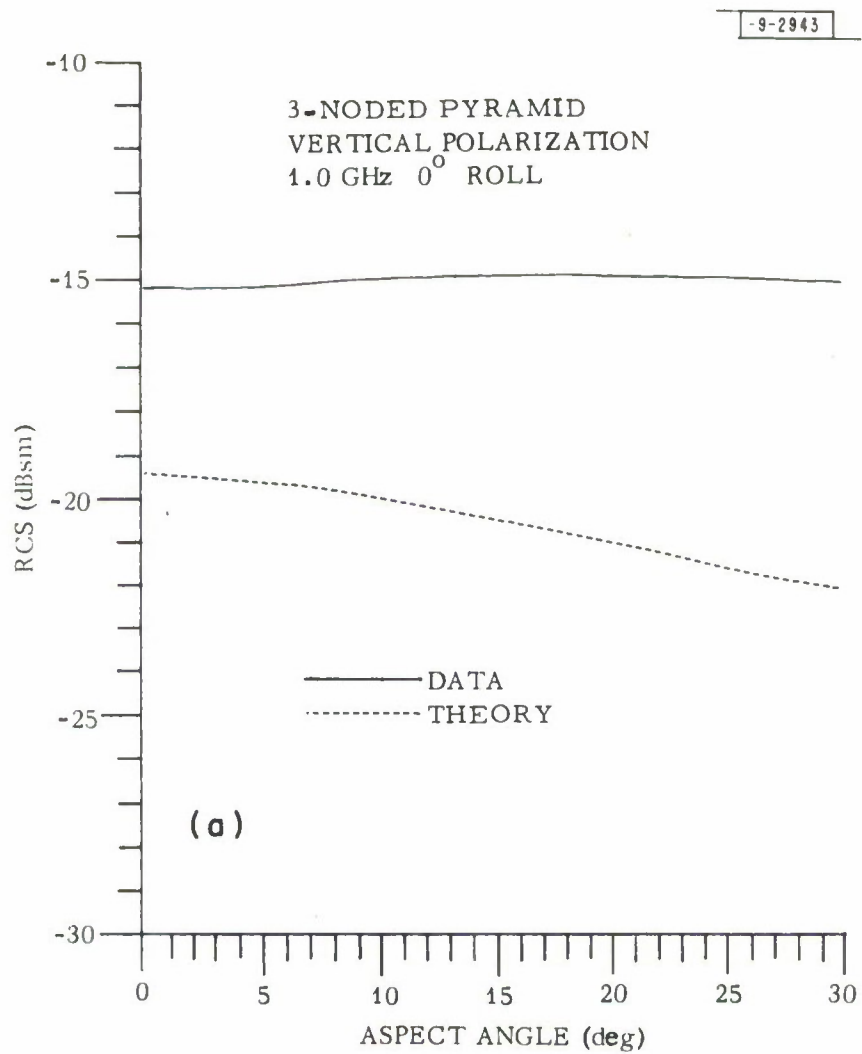


Fig. 10. Vertically polarized radar cross section of three-noded pyramid at 1.0 GHz.

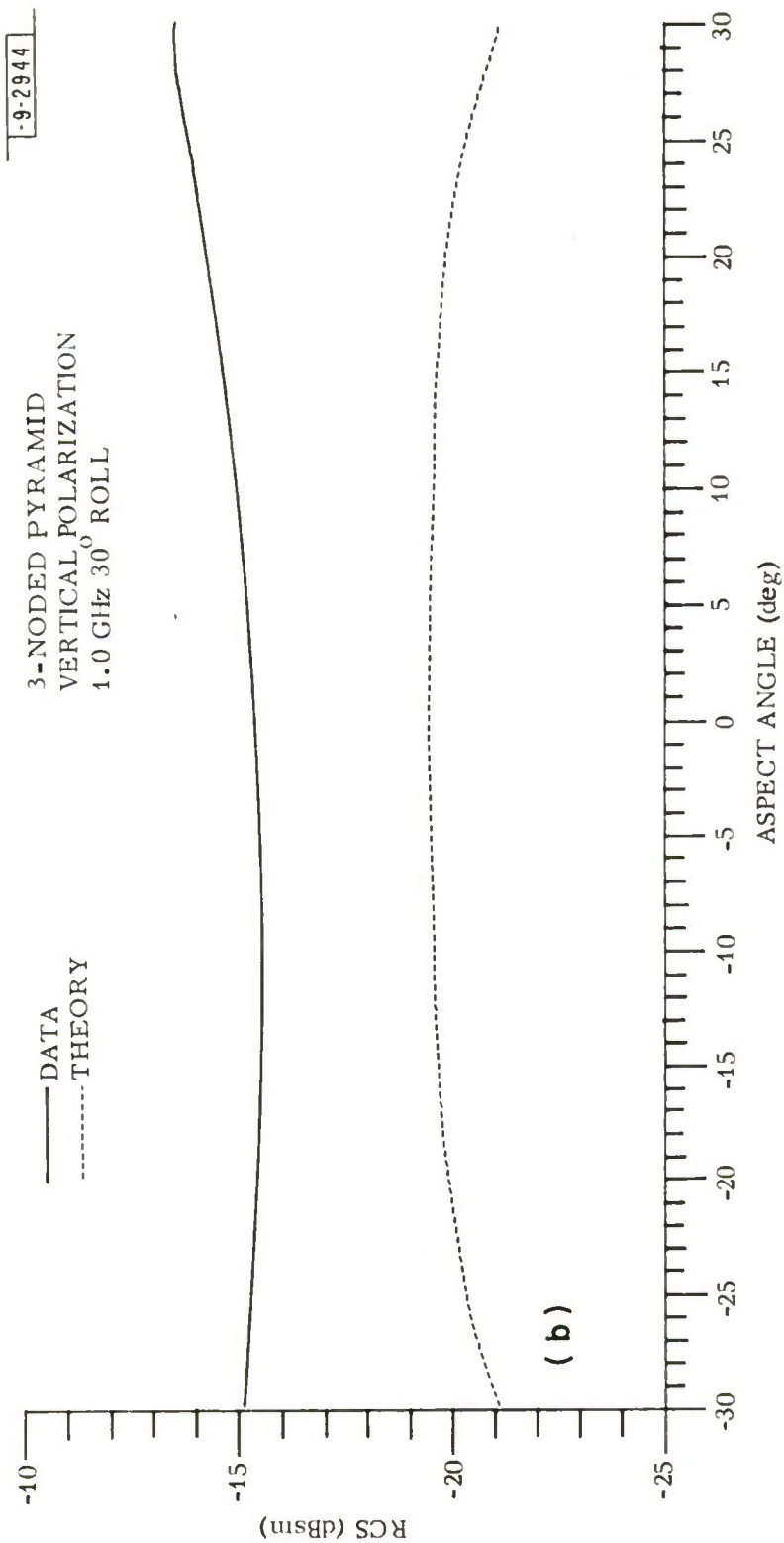


Fig. 10. Continued

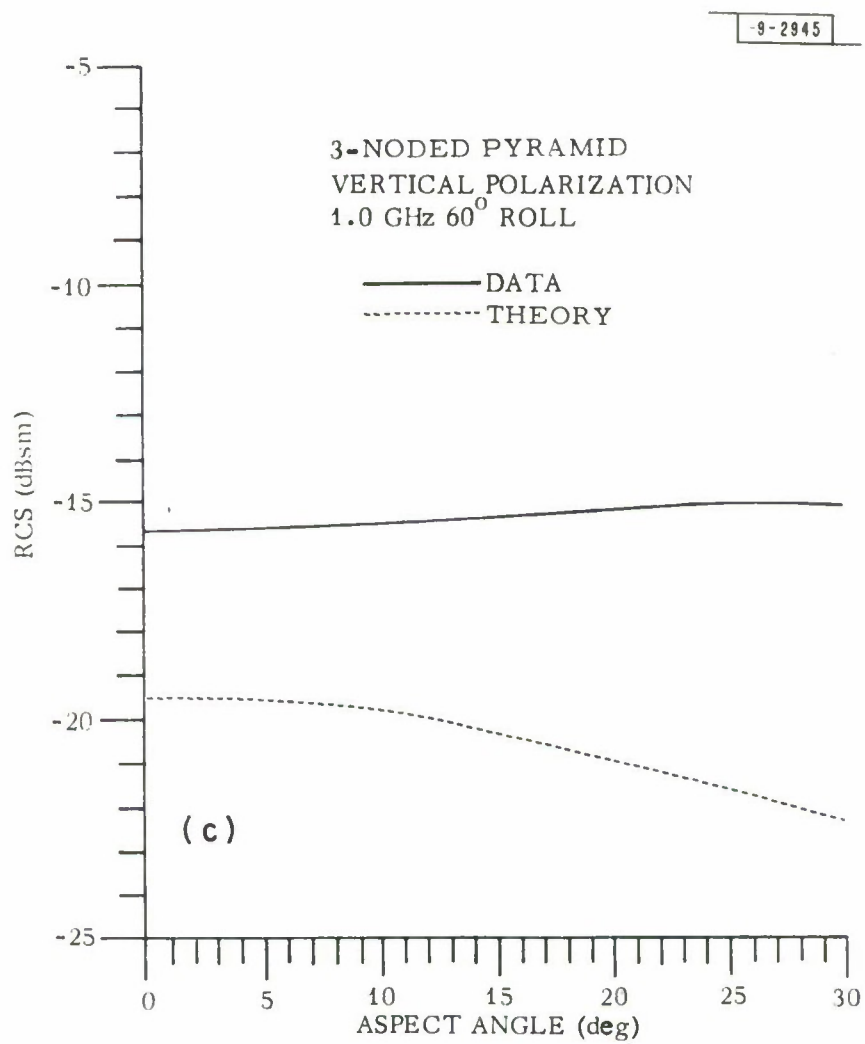


Fig. 10. Continued.

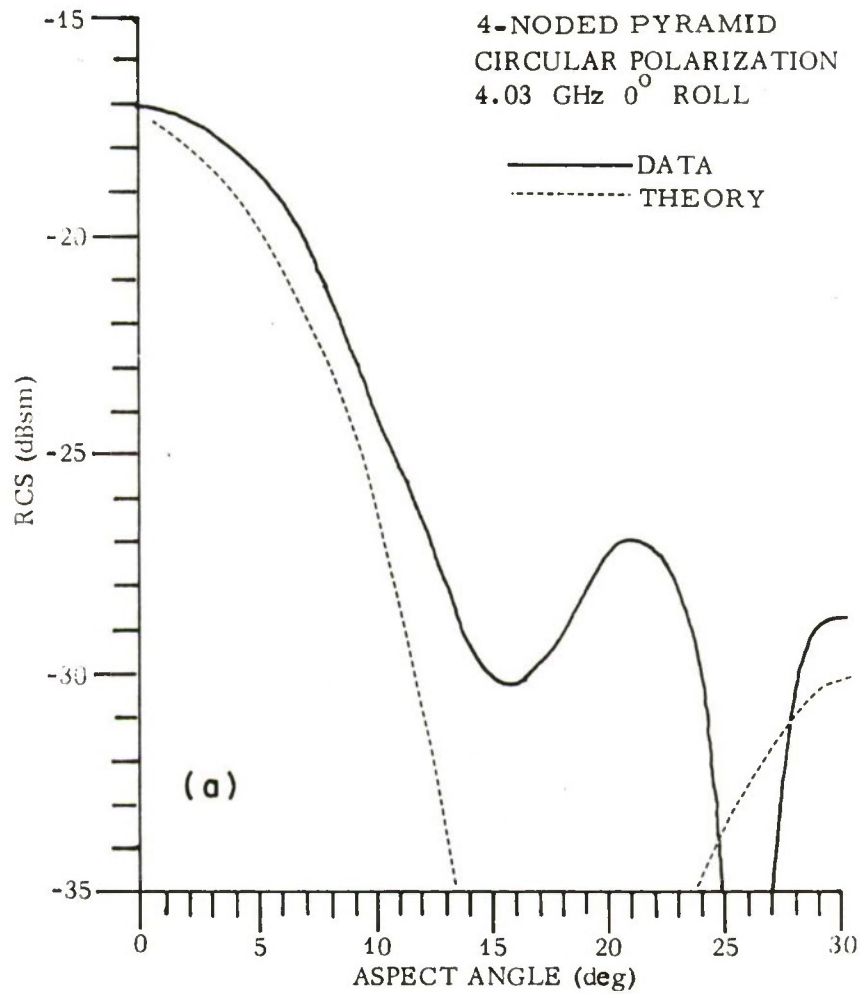


Fig. 11. Circularly polarized radar cross section of four-noded pyramid at 4.03 GHz.

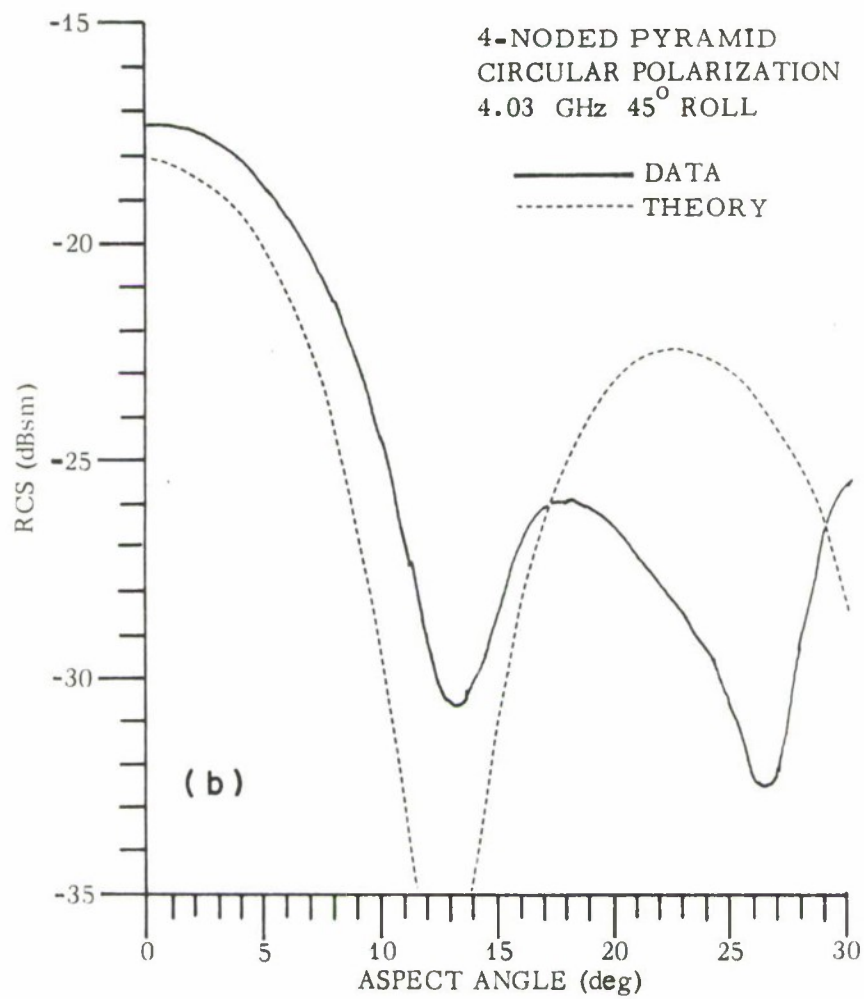


Fig. 11. Continued.

-9-2948

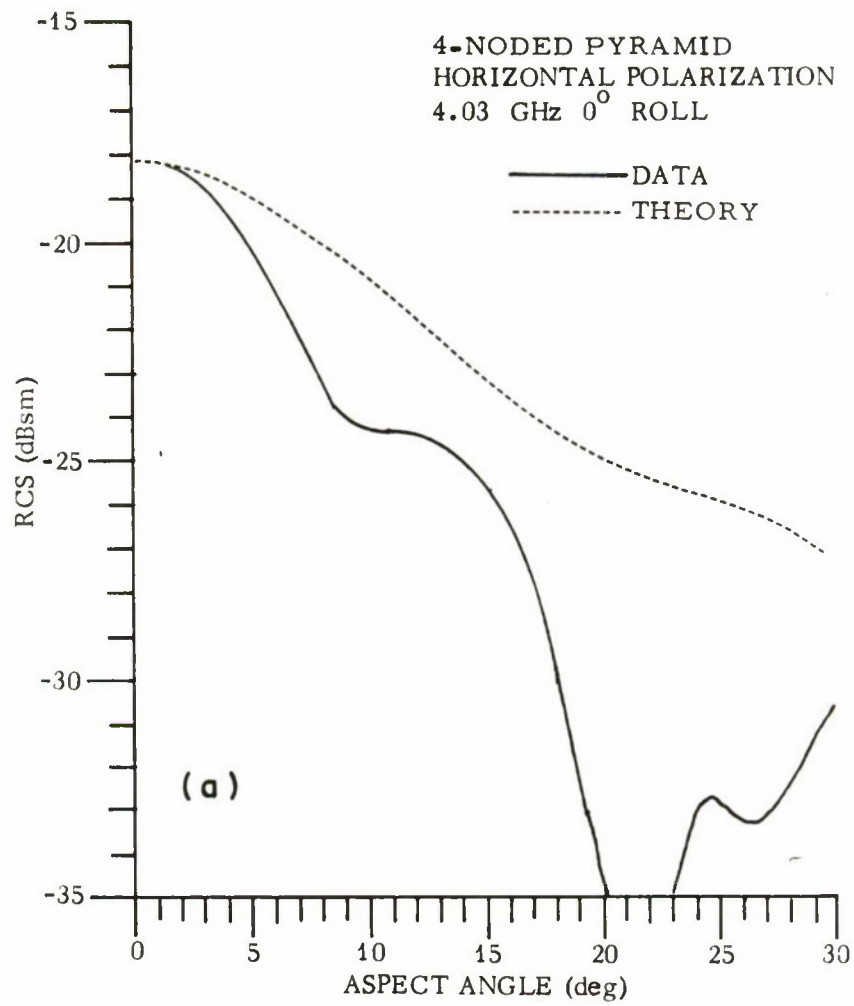


Fig. 12. Horizontally polarized radar cross section of four-noded pyramid at 4.03 GHz.

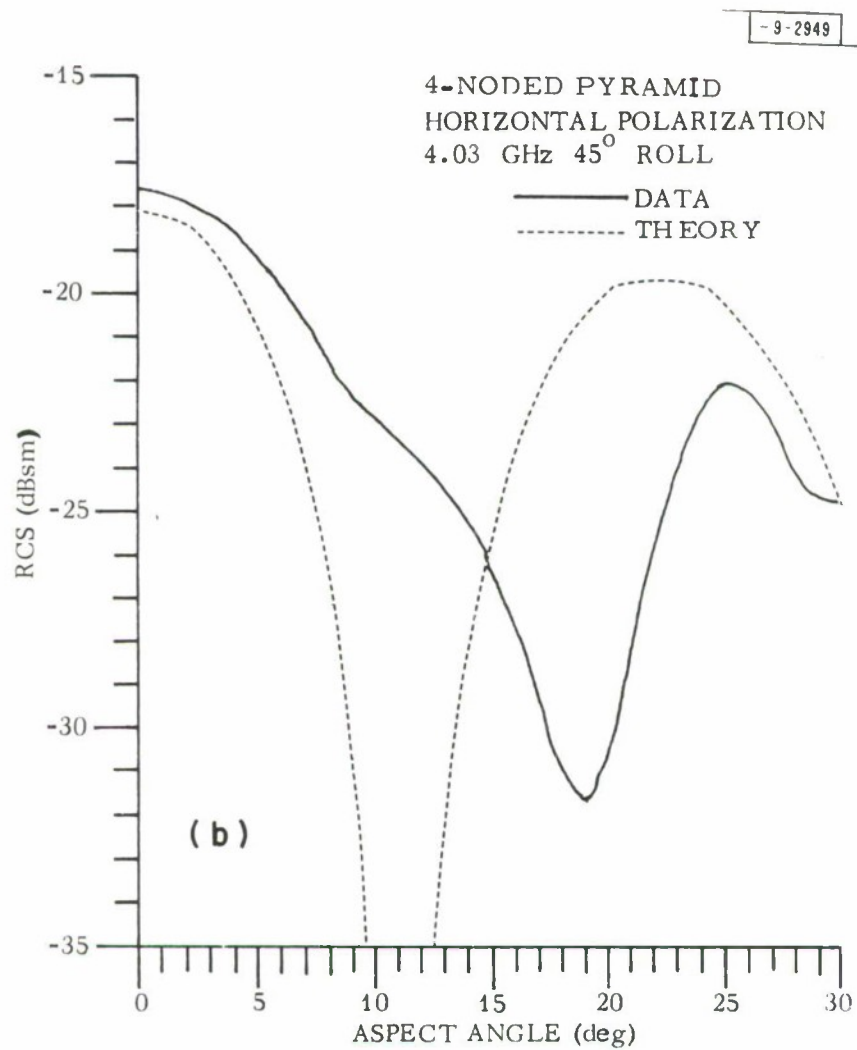


Fig. 12. Continued.

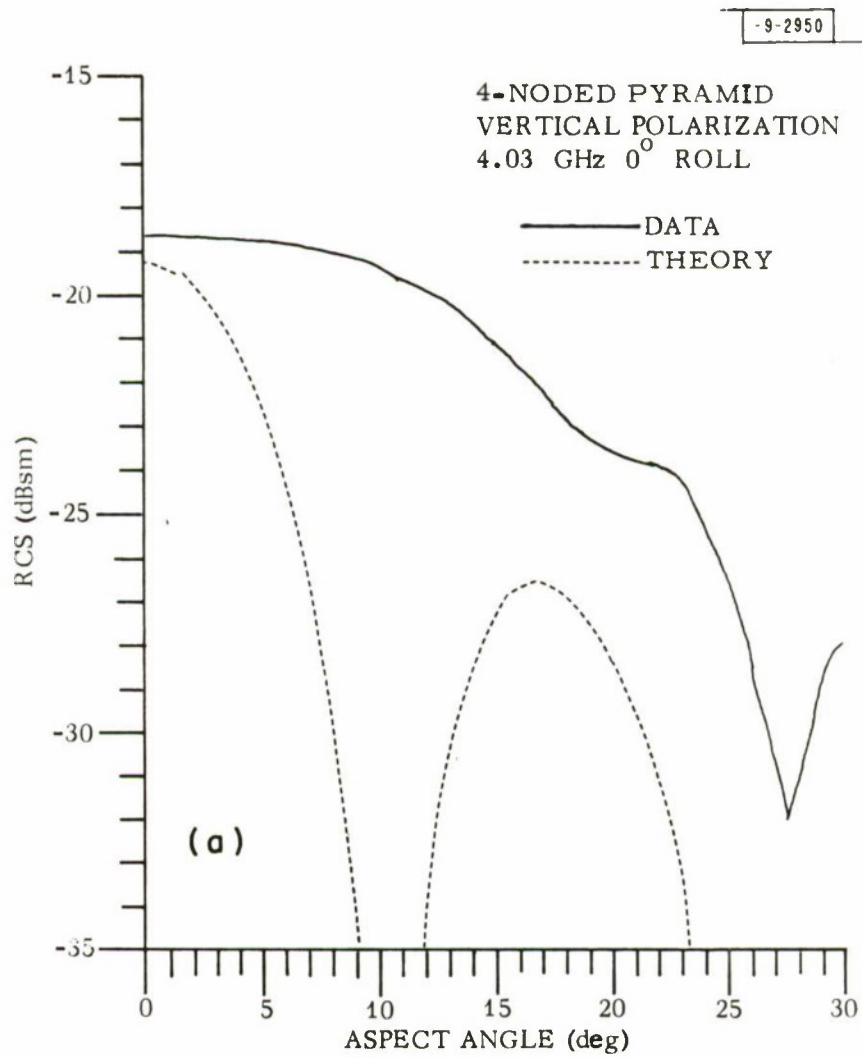


Fig. 13. Vertically polarized radar cross section of four-noded pyramid at 4.03 GHz.

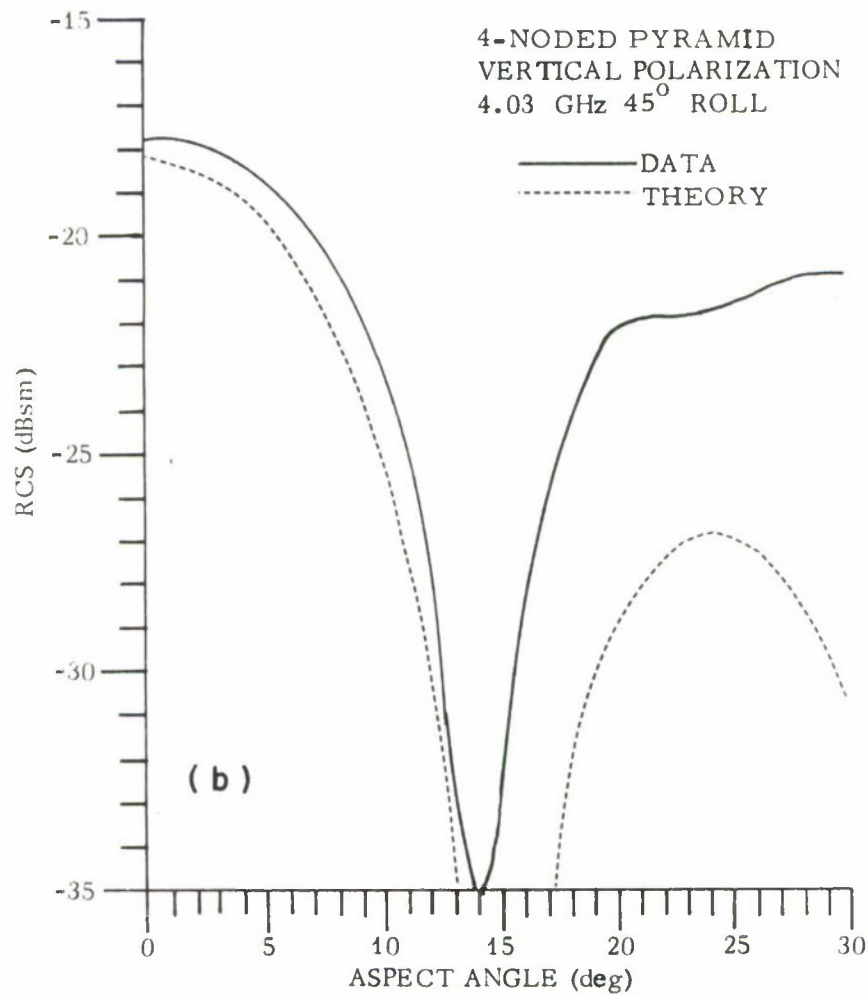


Fig. 13. Continued.

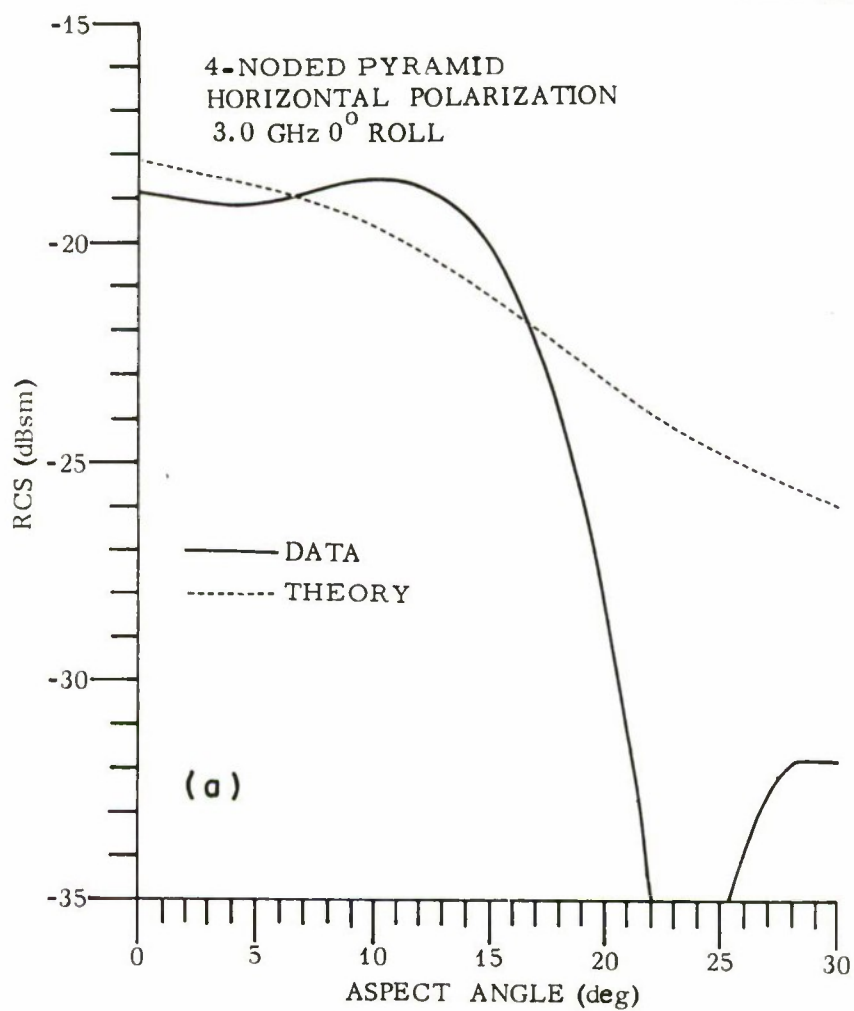


Fig. 14. Horizontally polarized radar cross section of four-noded pyramid at 3.0 GHz.

4-NODED PYRAMID
HORIZONTAL POLARIZATION
3.0 GHz 45° ROLL

-9-2953

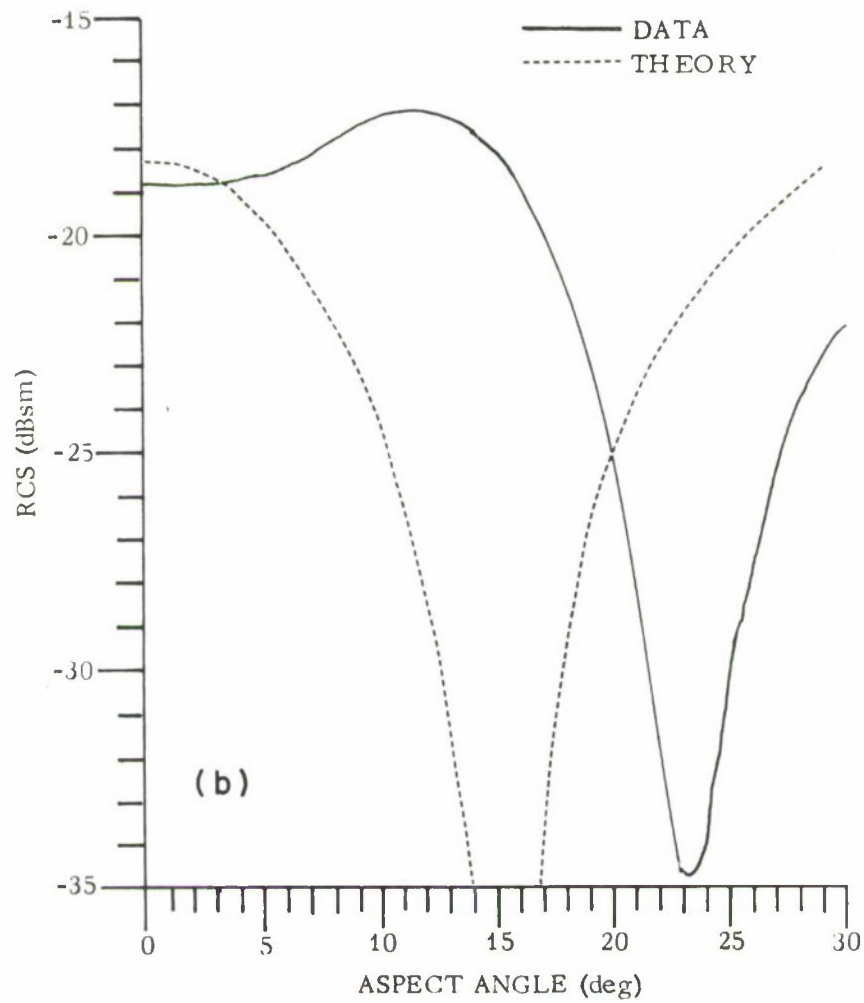


Fig. 14. Continued.

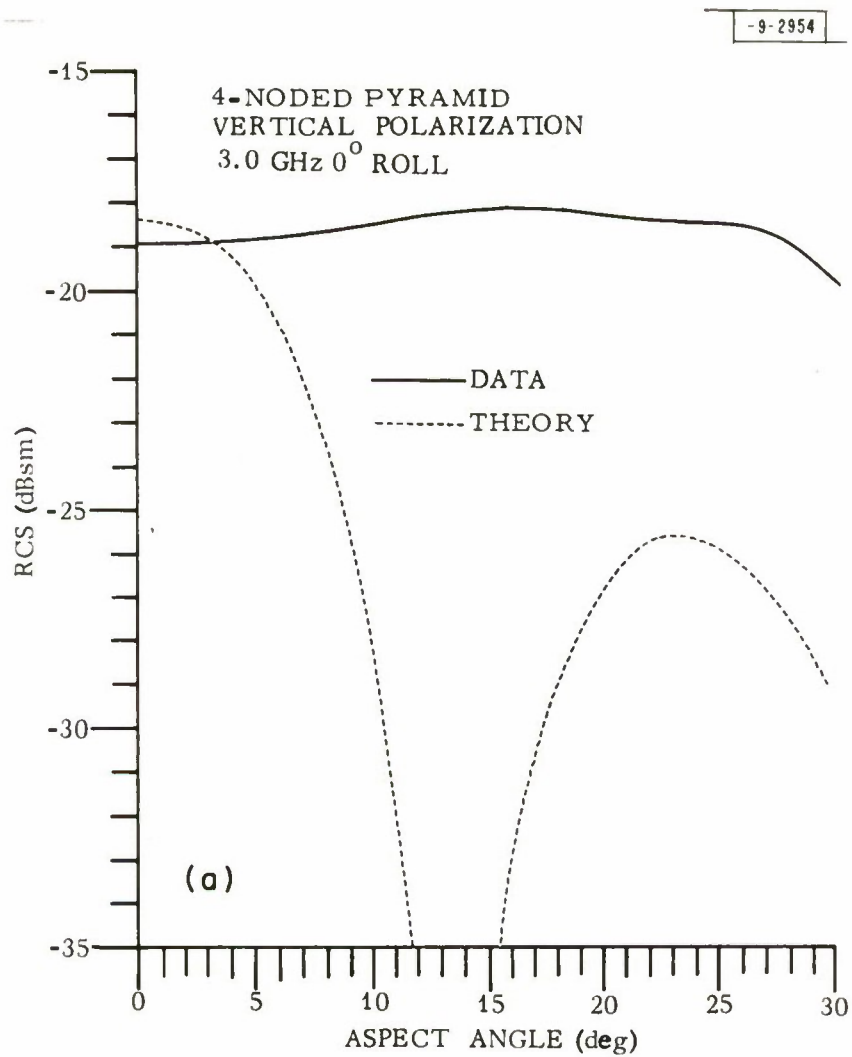


Fig. 15. Vertically polarized radar cross section of four-noded pyramid at 3.0 GHz.

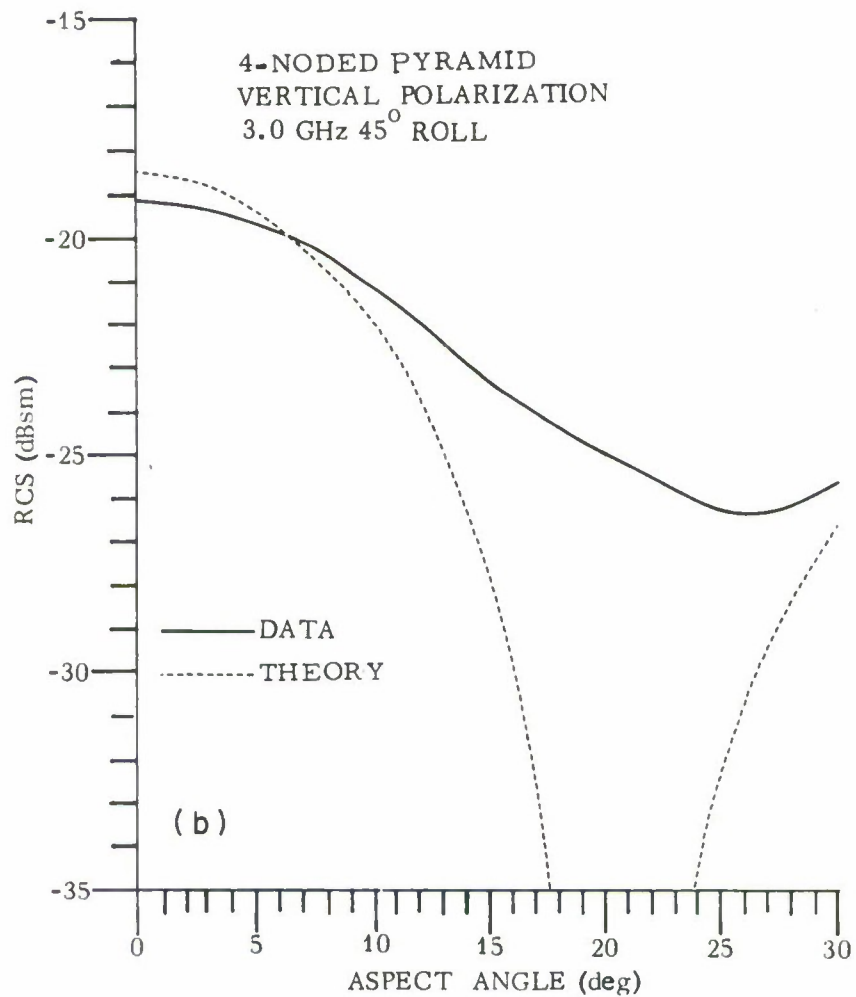


Fig. 15. Continued.

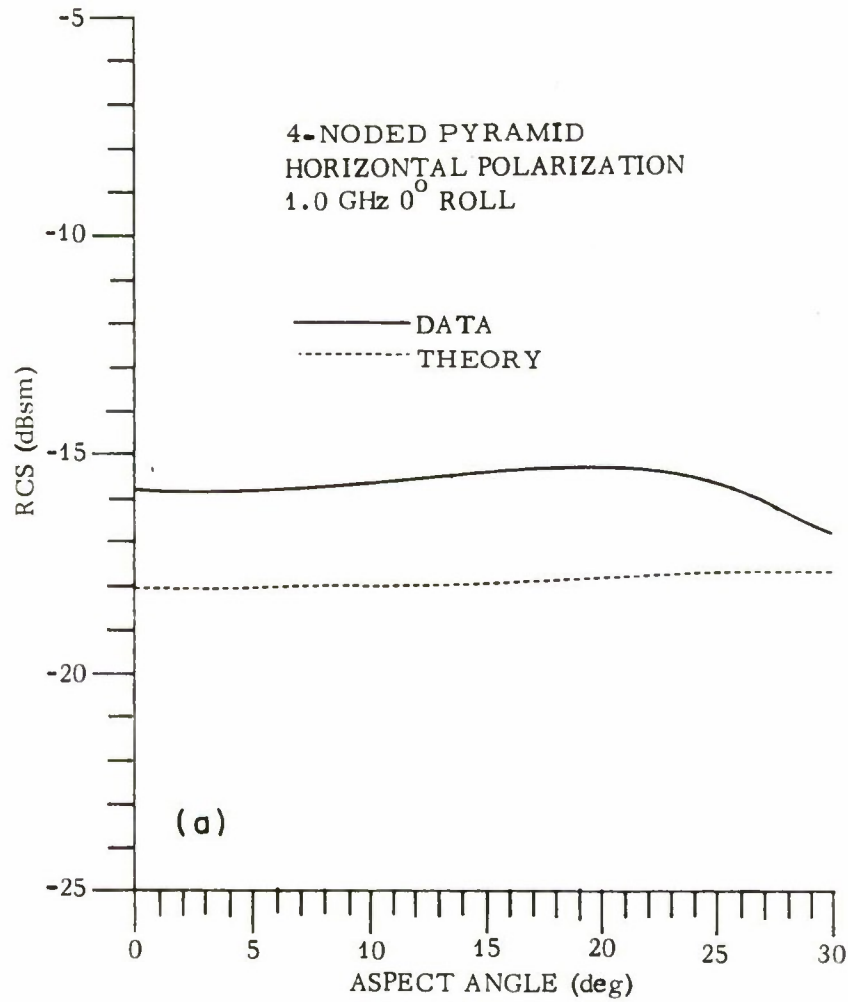


Fig. 16. Horizontally polarized radar cross section of four-noded pyramid at 1.0 GHz.

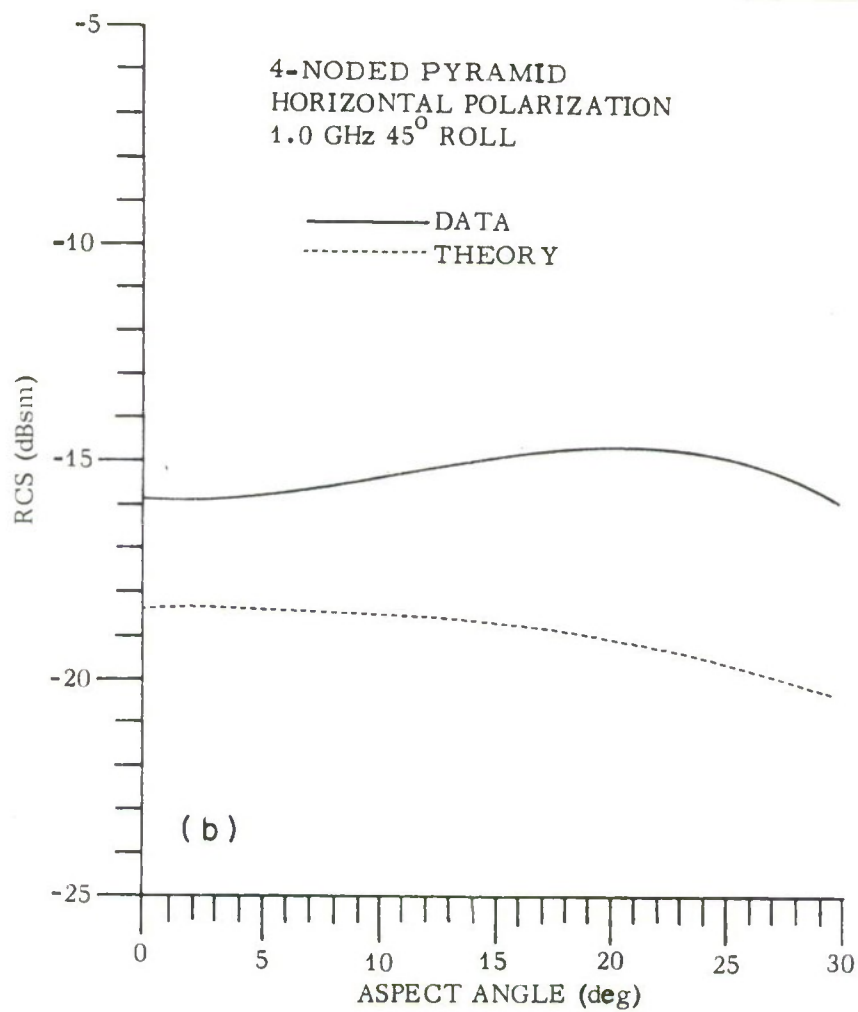


Fig. 16. Continued.

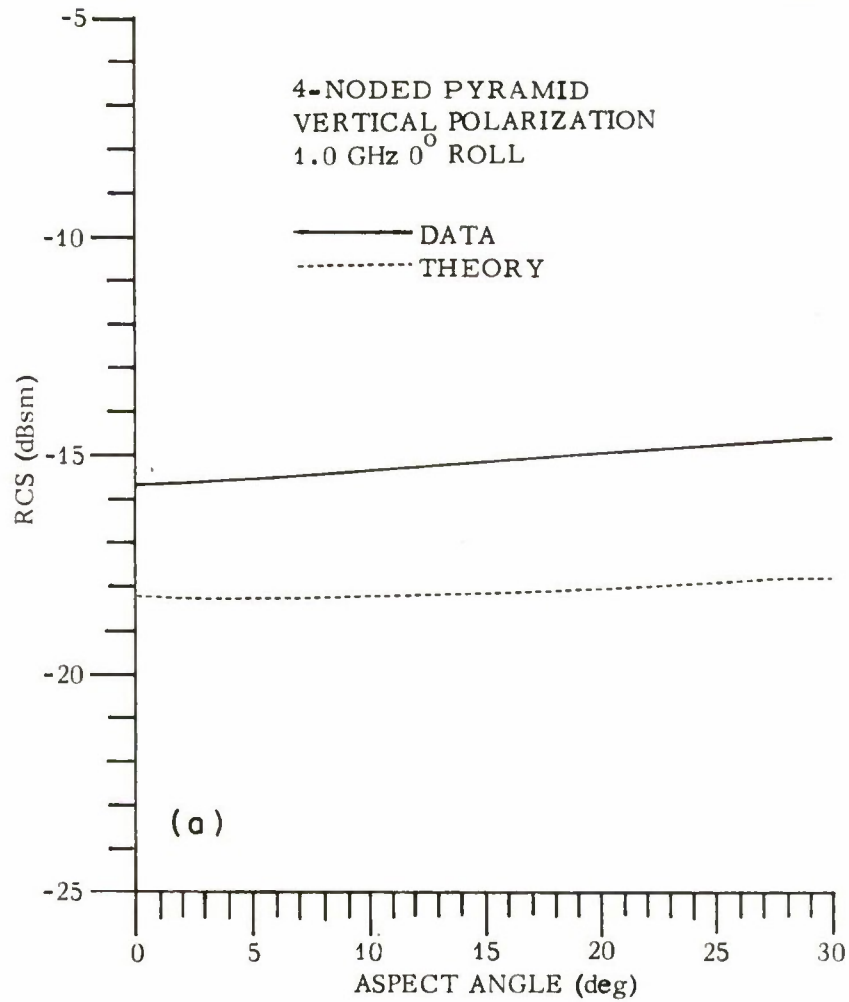


Fig. 17. Vertically polarized radar cross section of four-noded pyramid at 1.0 GHz.

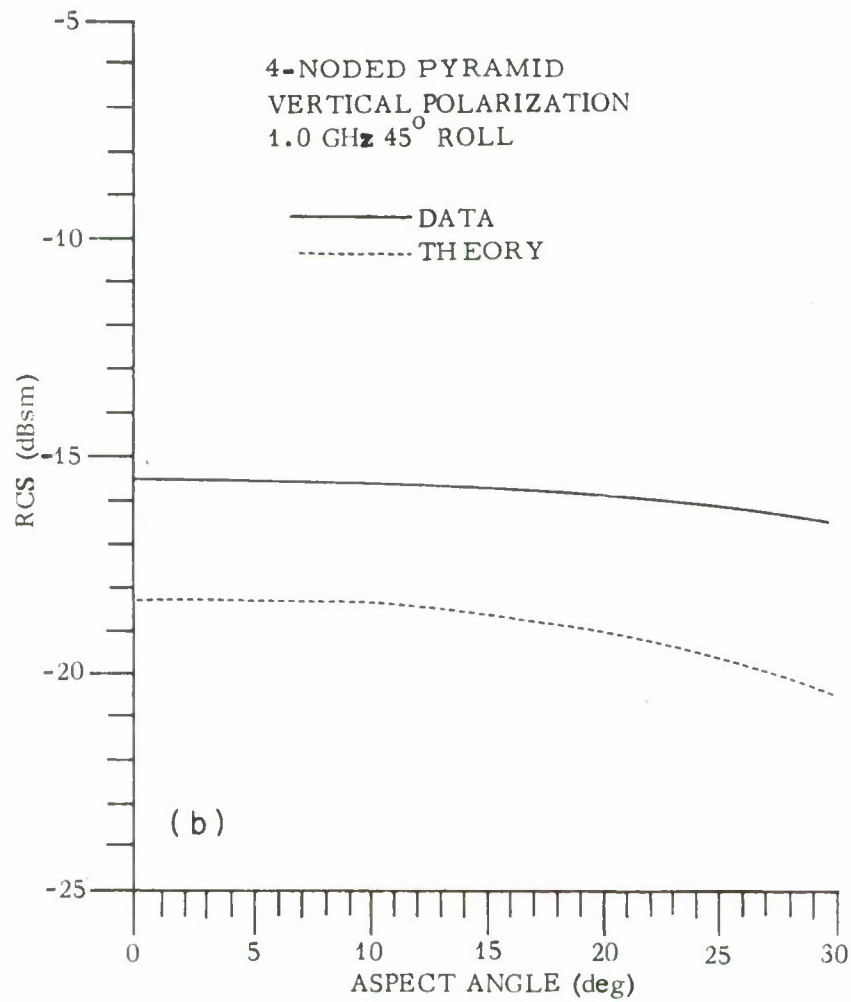


Fig. 17. Continued.

-9-2960

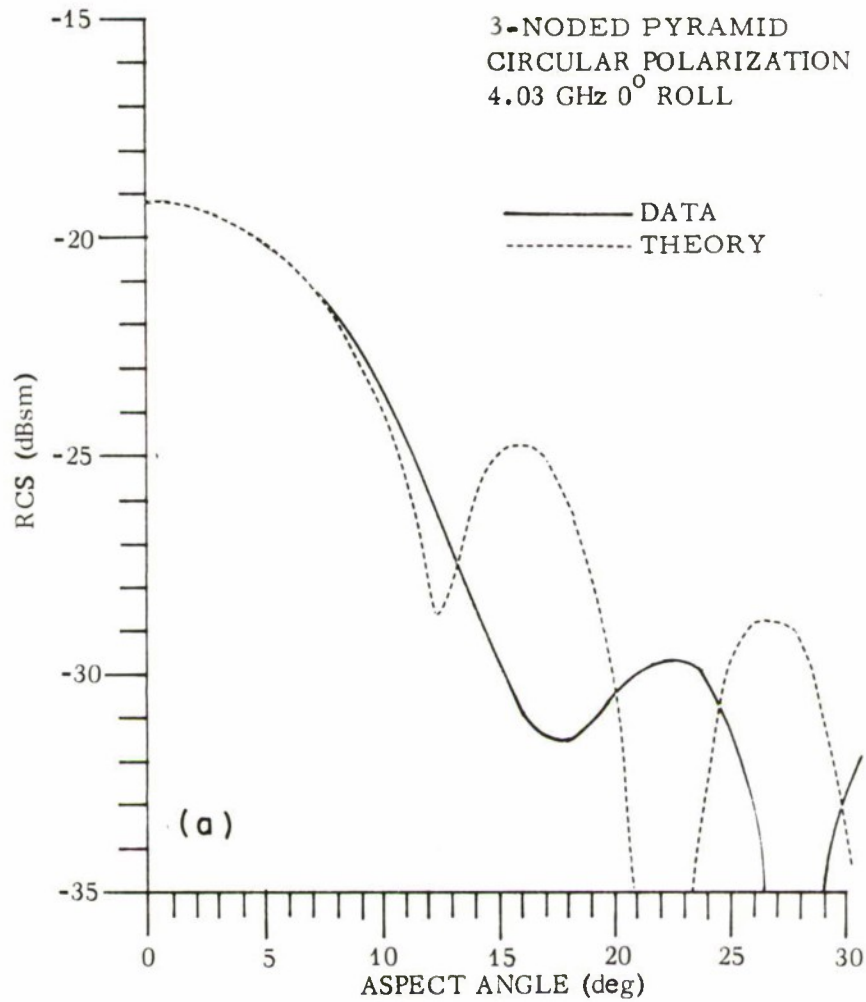


Fig. 18. Circularly polarized radar cross section of three-noded pyramid at 4.03 GHz.

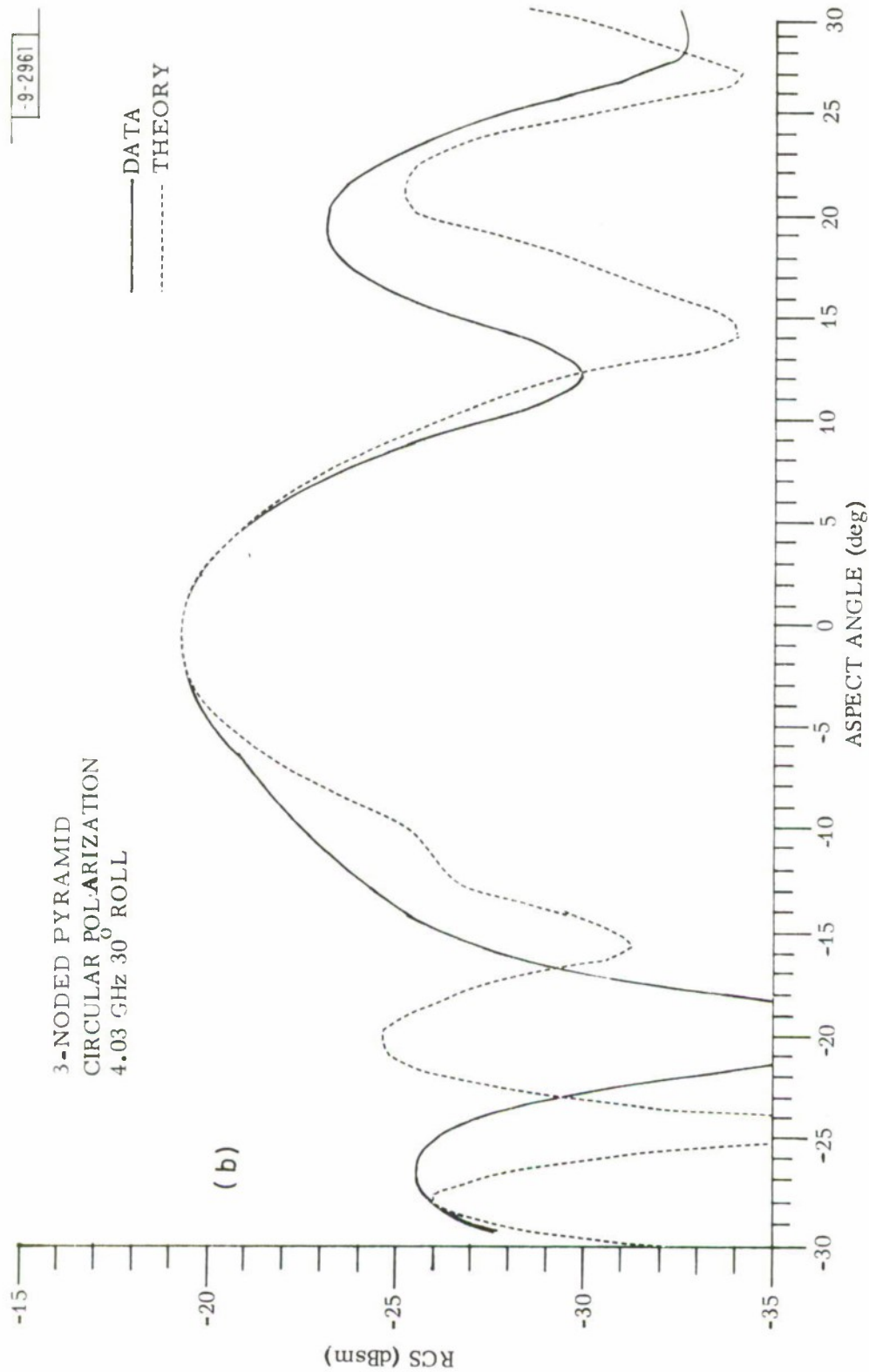


Fig. 18. Continued.

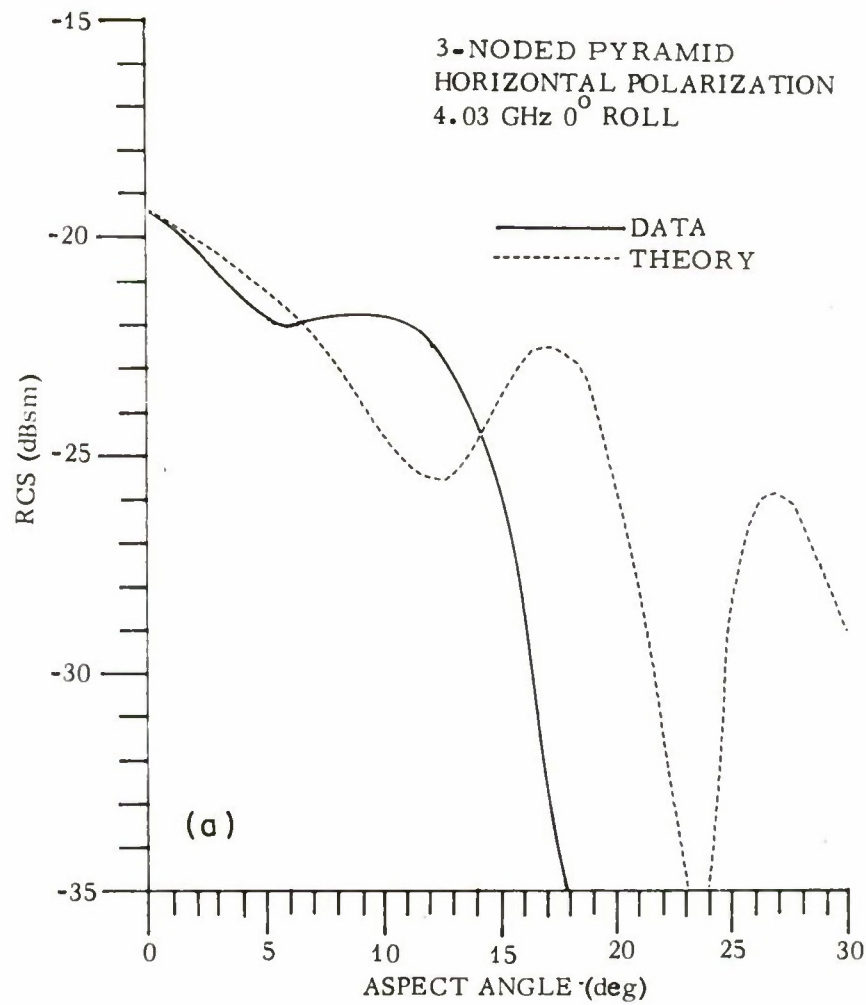


Fig. 19. Horizontally polarized radar cross section of three-noded pyramid at 4.03 GHz.

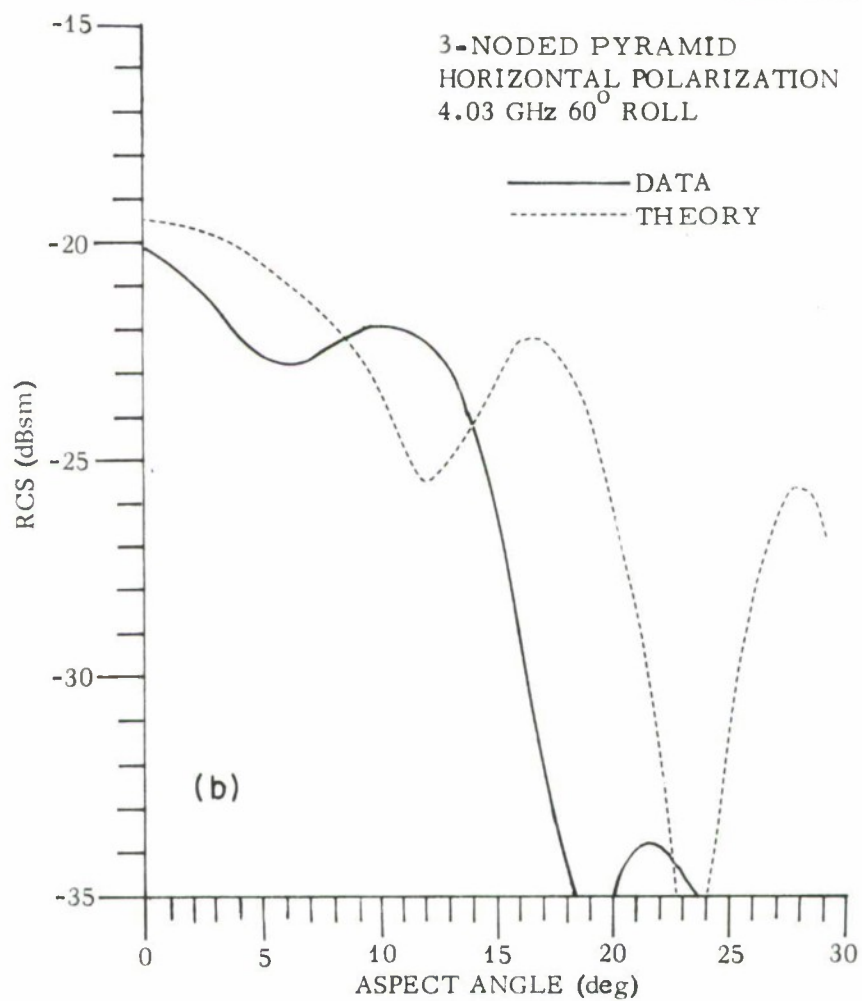


Fig. 19. Continued.

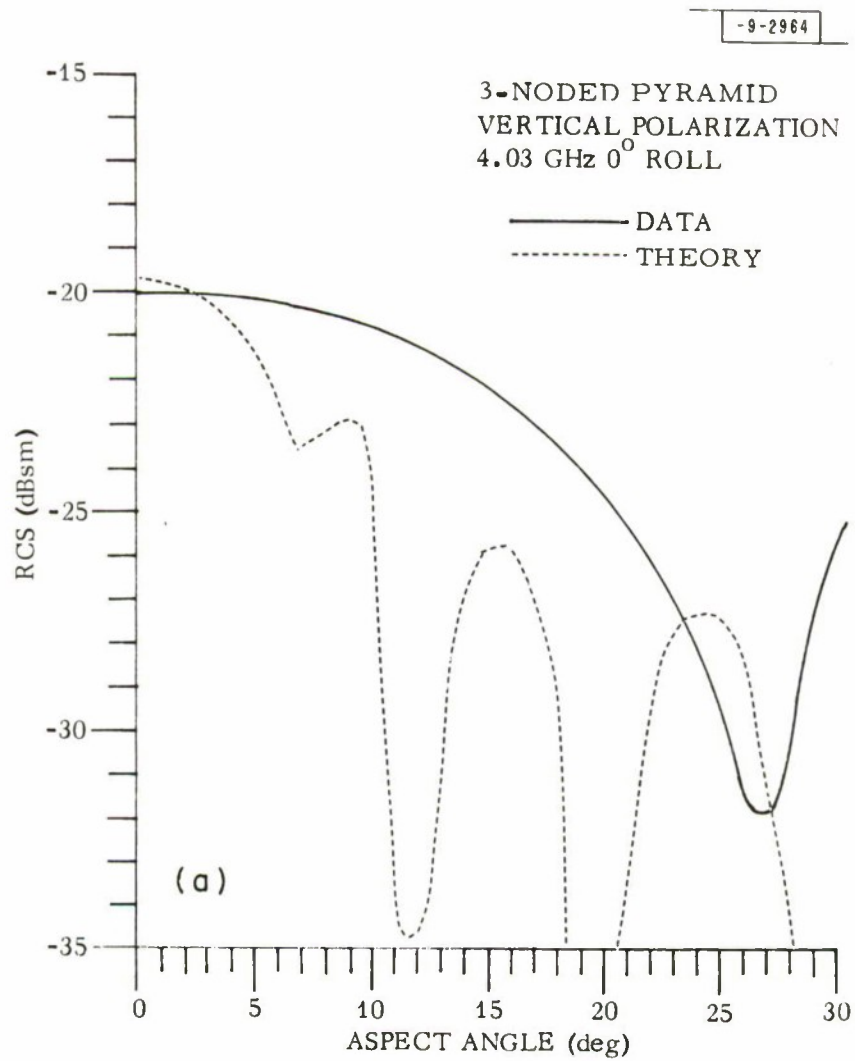


Fig. 20. Vertically polarized radar cross section of three-noded pyramid at 4.03 GHz.

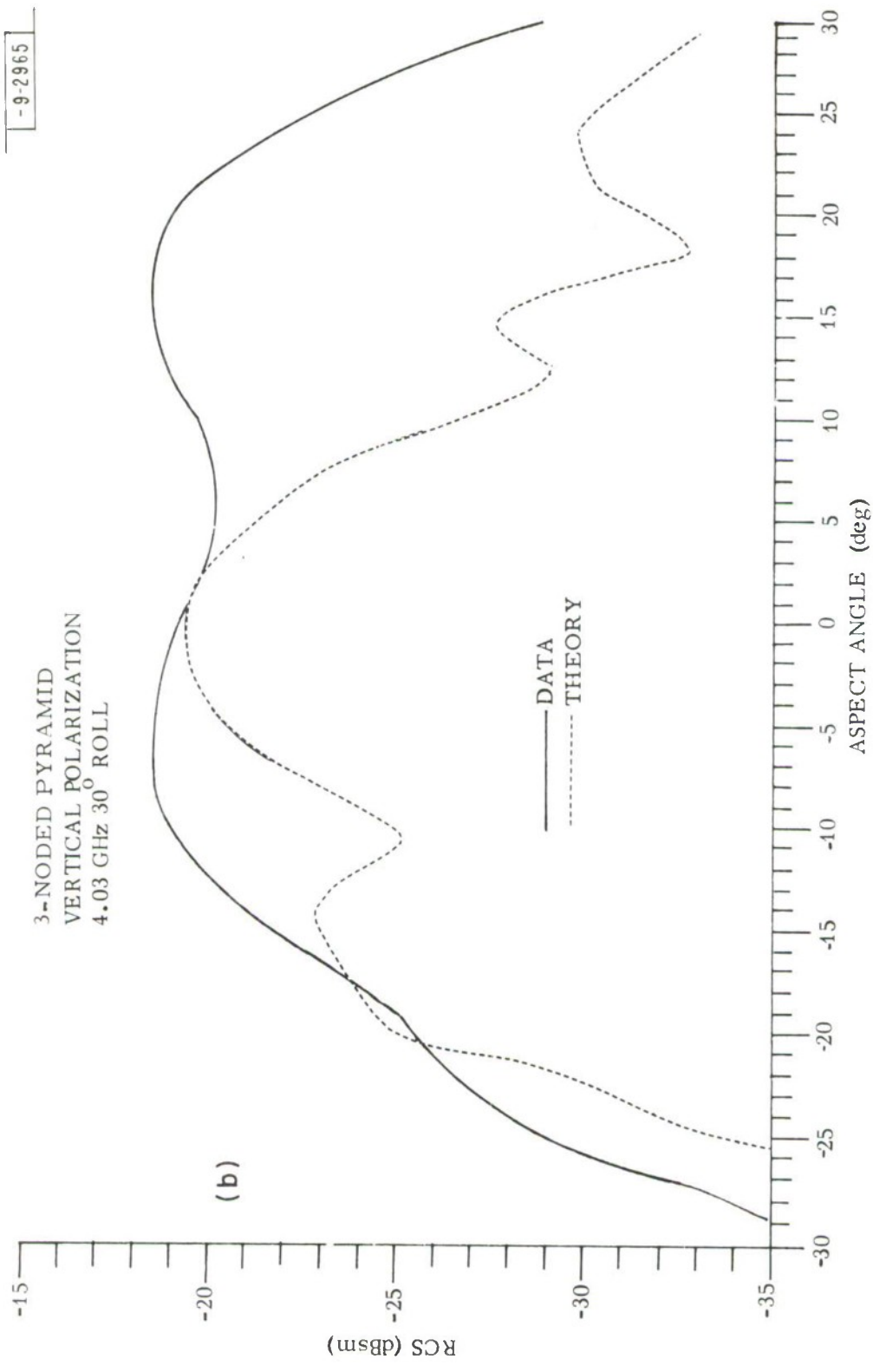


Fig. 20. Continued.

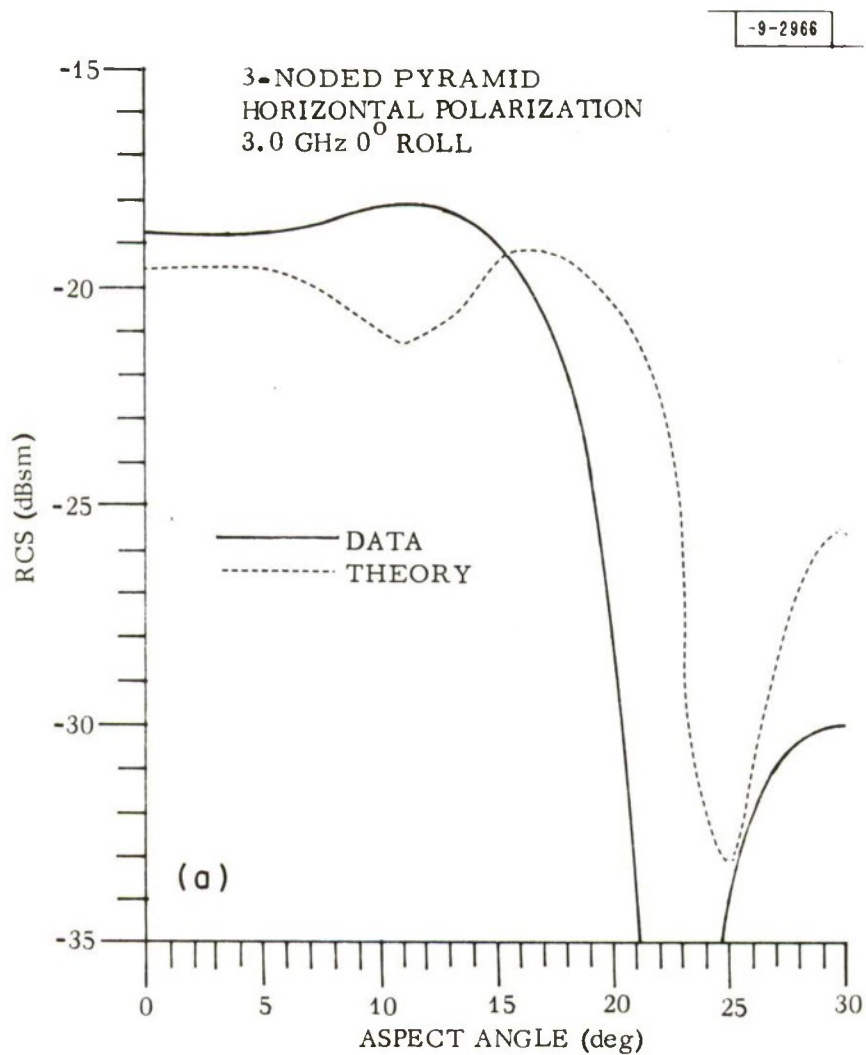


Fig. 21. Horizontally polarized radar cross section of three-noded pyramid at 3.0 GHz.

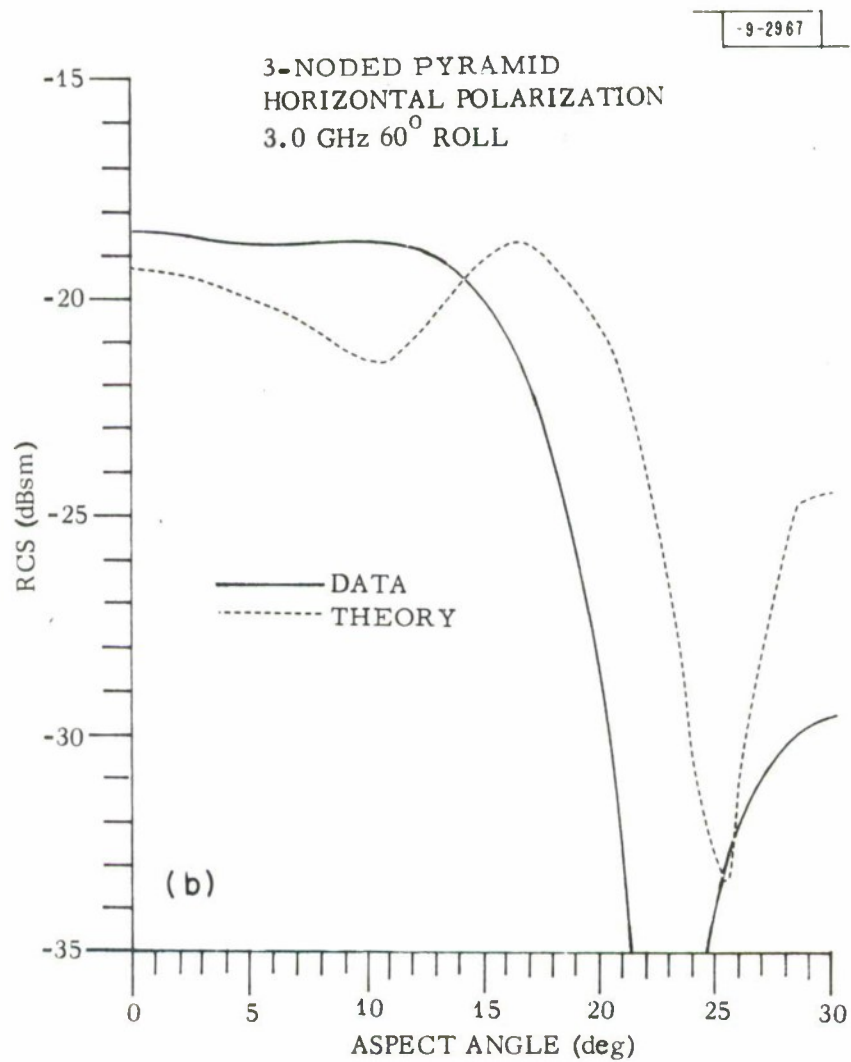


Fig. 21. Continued.

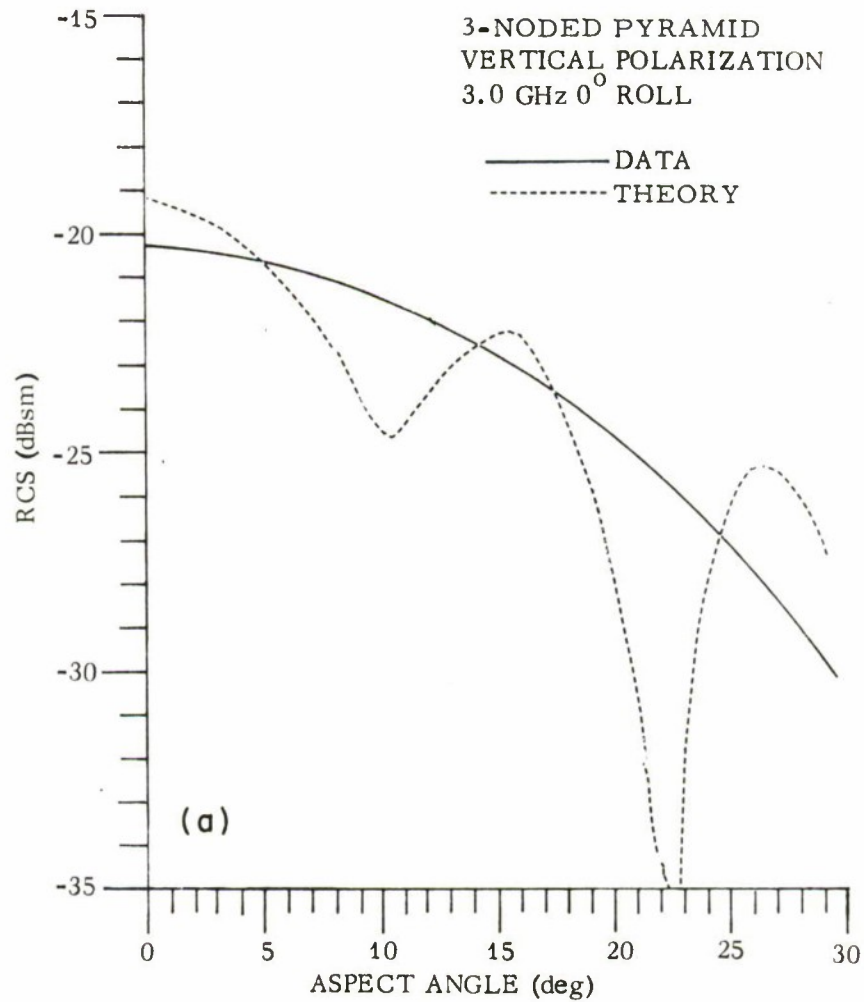


Fig. 22. Vertically polarized radar cross section of three-noded pyramid at 3.0 GHz.

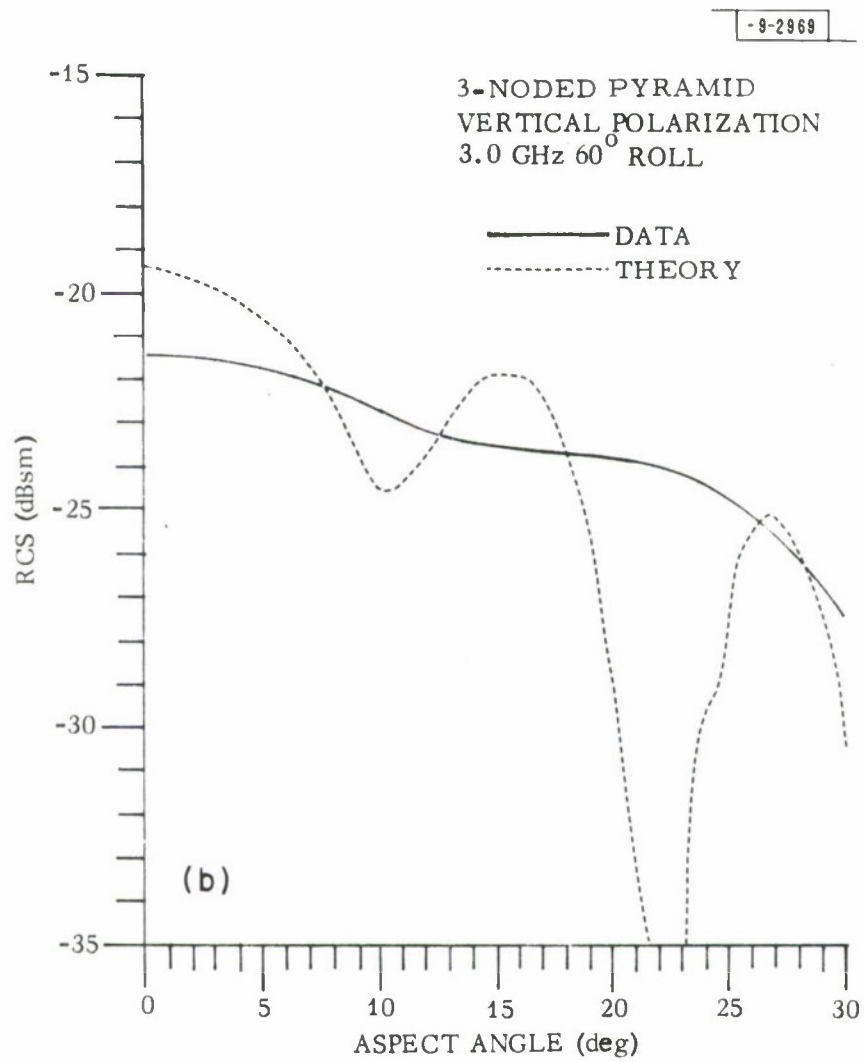


Fig. 22. Continued.

DOCUMENT CONTROL DATA - R&D

(Security classification of title, body of abstract and indexing annotation must be entered when the overall report is classified)

1. ORIGINATING ACTIVITY (Corporate author) Lincoln Laboratory, M.I.T.		2a. REPORT SECURITY CLASSIFICATION Unclassified	
		2b. GROUP None	
3. REPORT TITLE Radar Cross Section of a Pyramid with Nodes			
4. DESCRIPTIVE NOTES (Type of report and inclusive dates) Technical Note			
5. AUTHOR(S) (Last name, first name, initial) Schoendorf, William H.			
6. REPORT DATE 16 November 1972		7a. TOTAL NO. OF PAGES 82	7b. NO. OF REFS 5
8a. CONTRACT OR GRANT NO. F19628-73-C-0002		9a. ORIGINATOR'S REPORT NUMBER(S) Technical Note 1972-25	
b. PROJECT NO. 627A		9b. OTHER REPORT NO(S) (Any other numbers that may be assigned this report) ESD-TR-72-260	
c.			
d.			
10. AVAILABILITY/LIMITATION NOTICES Approved for public release; distribution unlimited.			
11. SUPPLEMENTARY NOTES None		12. SPONSORING MILITARY ACTIVITY Air Force Systems Command, USAF	
13. ABSTRACT <p>High-frequency scattering by a perfectly conducting N-noded pyramid is investigated. The principally polarized radar cross section is derived by integrating the fields scattered from a wedge around the base termination and, also, the longitudinal edges. The theoretical results are compared with measurements and shown to be in reasonable agreement.</p>			
14. KEY WORDS radar cross section conically shaped bodies nodes re-entry systems ray diffraction			